AGU PUBLICATIONS

JGR

Journal of Geophysical Research: Oceans

RESEARCH ARTICLE

10.1002/2015JC010878

Key Points:
- Multiplatform observations of a subsurface anticyclone formation off Peru
- Flow separation is suggested as the formation mechanism
- The eddy provides an important coastal open ocean exchange mechanism for solutes

Correspondence to:
S. Thomsen,
sthomsen@geomar.de

Citation:
Thomsen, S., T. Kanzow, G. Krahmann, R. J. Greatbatch, M. Dengler, and G. Lavik (2016), The formation of a subsurface anticyclonic eddy in the Peru-Chile Undercurrent and its impact on the near-coastal salinity, oxygen, and nutrient distributions, *J. Geophys. Res. Oceans*, *121*, 476–501, doi:10.1002/2015JC010878.

Received 28 MAR 2015
Accepted 11 DEC 2015
Accepted article online 18 DEC 2015
Published online 13 JAN 2016

The formation of a subsurface anticyclonic eddy in the Peru-Chile Undercurrent and its impact on the near-coastal salinity, oxygen, and nutrient distributions

Soeren Thomsen[1], Torsten Kanzow[1,2], Gerd Krahmann[1], Richard J. Greatbatch[1,3], Marcus Dengler[1], and Gaute Lavik[4]

[1]GEOMAR Helmholtz Centre for Ocean Research, Kiel, Germany, [2]Alfred-Wegener-Institute Helmholtz Centre for Polar and Marine Research, Bremerhaven, Germany, [3]Kiel University, Kiel, Faculty of Mathematics and Natural Sciences, Germany, [4]Max Planck Institute for Marine Microbiology, Bremen, Germany

Abstract The formation of a subsurface anticyclonic eddy in the Peru-Chile Undercurrent (PCUC) in January and February 2013 is investigated using a multiplatform four-dimensional observational approach. Research vessel, multiple glider, and mooring-based measurements were conducted in the Peruvian upwelling regime near 12°30′S. The data set consists of >10,000 glider profiles and repeated vessel-based hydrography and velocity transects. It allows a detailed description of the eddy formation and its impact on the near-coastal salinity, oxygen, and nutrient distributions. In early January, a strong PCUC with maximum poleward velocities of ~0.25 m/s at 100–200 m depth was observed. Starting on 20 January, a subsurface anticyclonic eddy developed in the PCUC downstream of a topographic bend, suggesting flow separation as the eddy formation mechanism. The eddy core waters exhibited oxygen concentration of <1 μmol/kg, an elevated nitrogen deficit of ~17 μmol/L, and potential vorticity close to zero, which seemed to originate from the bottom boundary layer of the continental slope. The eddy-induced across-shelf velocities resulted in an elevated exchange of water masses between the upper continental slope and the open ocean. Small-scale salinity and oxygen structures were formed by along-isopycnal stirring, and indications of eddy-driven oxygen ventilation of the upper oxygen minimum zone were observed. It is concluded that mesoscale stirring of solutes and the offshore transport of eddy core properties could provide an important coastal open ocean exchange mechanism with potentially large implications for nutrient budgets and biogeochemical cycling in the oxygen minimum zone off Peru.

1. Introduction

The Peruvian upwelling system is characterized by permanent Ekman-driven coastal upwelling forced by sustained trade winds largely parallel to the Peruvian coastline [*Strub et al.*, 1998]. The upwelling brings cold and nutrient-rich water to the surface, resulting in a band of low sea surface temperatures and high primary production along the coast [*Pennington et al.*, 2006]. It is one of the most productive areas of the world ocean and consequently of great economic and scientific interest. Despite covering only 0.1% of the world ocean surface, about 10% of the world fish catch occurs in the Peruvian upwelling system [*Chavez et al.*, 2008]. Being one of the four major eastern boundary upwelling systems, the Peruvian upwelling regime comprises one of the largest oxygen minimum zones (OMZs) [*Karstensen et al.*, 2008; *Fuenzalida et al.*, 2009; *Paulmier and Ruiz-Pino*, 2009]. A combination of poor ventilation of thermocline water masses and enhanced microbial subsurface respiration induced by high primary production and the associated export of organic matter results in an OMZ characterized by dissolved oxygen concentration of less than 1 μmol/kg [*Revsbech et al.*, 2009; *Kalvelage et al.*, 2013]. The oxycline depth off Peru is often very shallow and varies between 10 and 80 m [*Hamersley et al.*, 2007; *Gutiérrez et al.*, 2008]. Due to the low oxygen concentrations, the Peruvian upwelling system is considered to be an important region for oceanic nitrogen loss [*Cline and Richards*, 1972; *Codispoti and Packard*, 1980; *Hamersley et al.*, 2007; *Gruber*, 2008; *Lam et al.*, 2009].

The near-coastal current system off Peru is mostly wind driven [*Gunther*, 1936; *Strub et al.*, 1998]. Two currents, the Peru Coastal Current and the Peru-Chile Undercurrent (PCUC), are of relevance for this study. The Peru Coastal Current flows equatorward in the Ekman layer at the surface [*Penven et al.*, 2005]. Below this

surface current, the subsurface PCUC flows poleward with a mean core speed of 0.10–0.15 m/s at 100–150 m depth between 12°S and 15°S [*Wyrtki*, 1963, 1967; *Brink et al*., 1983; *Huyer et al*., 1991; *Strub et al*., 1998; *Penven et al*., 2005; *Kessler*, 2006; *Colas et al*., 2012; *Chaigneau et al*., 2013].

The Peruvian upwelling system encompasses pronounced mesoscale variability [*Penven et al*., 2005], which is the focus of this study. Based on 15 years of altimeter data, *Chaigneau et al*. [2008] show that coherent mesoscale eddies off Peru are generated near the coast and subsequently propagate westward. *Chaigneau et al*. [2013] use Argo float-based CTD data to show that anticyclones (cyclones) tend to have their cores located below (within) the thermocline. They suggest that anticyclones might be formed by instabilities of the PCUC and cyclones by instabilities of the equatorward surface currents. Based on regional eddy-resolving model simulations, *Colas et al*. [2012] find a skewness of vorticity toward anticyclonic rotation between 100 and 150 m depth off Peru. The authors relate this vorticity dominance to subsurface anticyclonic coherent vortices and suggest that they arise from instability of the PCUC. These eddies, traditionally referred to as submesoscale coherent vortices, may exhibit a wide range of sizes. Yet they are in general smaller than the first baroclinic Rossby radius of deformation [*McWilliams*, 1985]. Different nomenclatures for subsurface anticyclonic eddies with convex lense-shaped density field found off Peru and Chile have been used in the recent literature, e.g., equatorial Pacific 13° water eddies [*Johnson and McTaggart*, 2010], subsurface anticyclonic coherent vortices [*Colas et al*., 2012], intrathermocline eddies [*Hormazabal et al*., 2013; *Combes et al*., 2015], and mode-water eddies [*Stramma et al*., 2013]. Here we use the term subsurface anticyclonic eddy because two important eddy characteristics are automatically defined with this term.

Submesoscale coherent vortices are observed at various places in the world ocean [*McDowell and Rossby*, 1978; *D'Asaro*, 1988; *Karstensen et al*., 2015; *Bosse et al*., 2015] and are often shed by boundary currents near sharp topographic bends [*Bower et al*., 1995, 1997; *Bosse et al*., 2015; *Molemaker et al*., 2015]. Their generation mechanism is puzzling and studies investigating this phenomenon have a long history [*McWilliams*, 1985; *D'Asaro*, 1988; *Prater*, 1992]. Based on submesoscale-resolving model simulations, *Molemaker et al*. [2015] shows the complexity of the eddy generation mechanism. It includes flow separation, upscale transport of kinetic energy, submesoscale instabilities, and small-scale dissipation. The study further highlights the important role of the dissipative bottom boundary layer for the generation of anticyclonic vorticity and of low potential vorticity water, which is found in the core of these eddies. These aspects have also been suggested in the conceptual model of *D'Asaro* [1988].

Mesoscale eddies have large effects on the horizontal and vertical transport of momentum, heat, and tracers [*Klein and Lapeyre*, 2009]. They strongly influence the near-surface chlorophyll distribution and biological productivity through various mechanisms and can enhance biological production in low-nutrient regions [*Jenkins*, 1988; *Falkowski et al*., 1991; *McGillicuddy et al*., 1998; *Oschlies and Garcon*, 1998; *McGillicuddy et al*., 2007; *Gaube et al*., 2014]. In eastern boundary upwelling regions, eddies are thought to induce a net reduction of biological productivity by exporting nutrients from the productive near-coastal region into the open ocean [*Rossi et al*., 2008, 2009; *Lathuilière et al*., 2010; *Gruber et al*., 2011].

OMZs are characterized by a sluggish mean circulation and thus mesoscale eddies are important for ventilating OMZs by means of along-isopycnal stirring [*Wyrtki*, 1962; *Luyten et al*., 1983a, 1983b; *Stramma et al*., 2010; *Hahn et al*., 2014; *Brandt et al*., 2015]. *Holte et al*. [2013] describe the vertical structure of cyclones and anticyclones in the southeast Pacific based on in situ measurements. They find that both types of eddies may trap coastal waters and transport them toward the open ocean. Subsurface anticyclonic eddies originating from the continental margin found in the open ocean OMZ off Peru and Chile can exhibit distinct physical and biogeochemical water mass anomalies such as low oxygen concentrations and elevated nitrogen deficits [*Stramma et al*., 2013, 2014]. *Kalvelage et al*. [2013] carried out nitrogen budget calculations based on nutrient measurements, experimentally determined nitrogen transformation rates and modeled export production for the eastern tropical South Pacific. They state that a large export of nitrogen deficient shelf waters into the open ocean OMZ is required to close their nitrogen budget. Near-coastal observations showing the eddy formation together with its initial physical and biogeochemical properties and subsequently the impact of these eddies on the near-coastal OMZ have, however, until now not been available.

This study is based on multiplatform observations including research vessel, glider, and mooring-based measurements carried out off Peru near 12°30′S in January and February 2013. The extensive data set allows a detailed high-resolution four-dimensional description of the formation of a subsurface

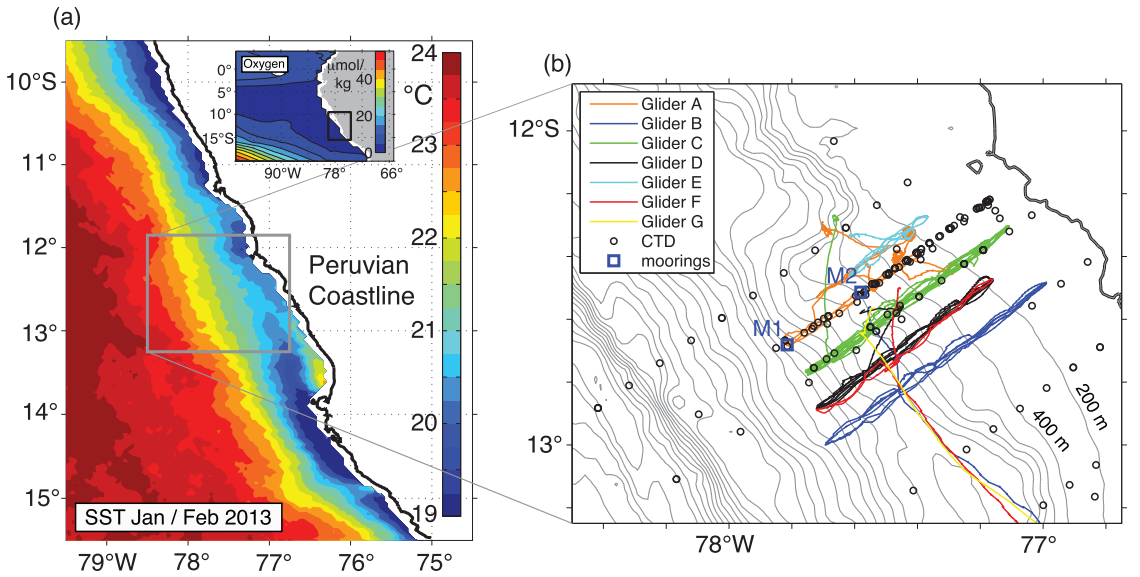

Figure 1. (a) Mean sea surface temperature off Peru during January and February 2013 from remote sensing (Modis Aqua/Terra) is color shaded (large plot). The small inlet shows oxygen concentration in μmol/kg in the eastern tropical Pacific at σ_θ=26.8 kg/m^3 as obtained from the MIMOC climatology [*Schmidtko et al.*, 2013] (small inlet). (b) The water depth (gray contours, 200 m interval), glider tracks (colored lines), conductivity temperature and depth (CTD) stations (black circles), and the two mooring positions (blue squares).

anticyclonic eddy occurring in the study area and its impact on the distribution of properties in the water column along the continental margin. The paper is structured as follows. In the next section, the different data sets used in this study and the data processing are explained. The oceanographic setting is described in section 3.1. Subsequently, the eddy formation chronology is shown in section 3.2 and the formation mechanism is discussed in section 3.3. In section 3.4, the changes in the salinity and oxygen distributions are directly related to the changing horizontal flow field, including the role of the eddy for the ventilation of the near-coastal OMZ off Peru. In section 3.5, we investigate the impact of the horizontal circulation on the nutrient distribution. In section 4, we discuss our results and relate them to other recent studies. This is followed by a short summary and conclusions in section 5.

2. Data and Methods

In January and February 2013, a multiplatform four-dimensional observational experiment was conducted in the Peruvian upwelling system between 12°S and 14°S to investigate the near-coastal mesoscale and submesoscale variability. In this study, we focus on measurements conducted in an area of ~100 km by ~100 km centered near 12°30′S (Figure 1). The experiment was carried out in the framework of the interdisciplinary "SFB 754 Climate-Biogeochemistry Interactions in the Tropical Ocean" project and included research vessel, multiple glider, and mooring-based measurements.

A multiple glider survey with seven Slocum gliders (Teledyne Webb Research) is the central component of the multiplatform approach [*Rudnick et al.*, 2004; *Testor et al.*, 2010]. The first glider was deployed 7 January 2013 during the R/V Meteor cruise 92 (M92, 5 January to 3 February) and the last glider was recovered 1 March 2013 during the R/V Meteor cruise 93 (M93, 7 February to 9 March). See Table 1 for more details.

Table 1. Glider Acronyms, Measurement Periods, Number of Profiles, and Maximum Diving Depth[a]

Glider	Measurement Period	Profiles	Max. Depth (m)
A	7–25 Jan, 27 Jan to 28 Feb	2593	450
B	18 Jan to 16 Feb	2599	200
C	7 Jan to 1 Mar	3099	200
D	24 Jan to 18 Feb	1042	735
E	15–25 Jan	480	450
F	17–30 Jan	761	305
G	16–20 Jan	179	305

[a]Please note that for gliders B, F, and G only profiles and maximum diving depths during their presence north of 13°15′S have been considered.

A conductivity, temperature, and depth (CTD) cell is mounted on each glider operating at a sampling rate of 1 Hz. Most gliders are equipped with an unpumped CTD (glider G used a pumped CTD).

Therefore, it is important to correct for the thermal mass of the conductivity cell in order to obtain reliable salinities [*Johnson et al*., 2007]. In this study, two methods are combined to provide the correction, which depends on the flushing rate of the conductivity cell, which in turn depends on the glider's speed through the water. The thermal mass correction by *Garau et al*. [2011] is applied, however using a modeled velocity, instead of the glider velocity, calculated from the temporal derivative of pressure. This modeled velocity is estimated using the flight model of *Merckelbach et al*. [2010]. This approach eliminates the influence vertical motion of the glider stemming from internal waves. These vertical motions are observed by the glider's pressure sensor but are not associated with forward movements of the glider. Thus, they do not lead to changes of the flushing rate used for the thermal mass correction. Internal wave motion is large in the coastal zone of the study area. Parameters such as conservative temperature, absolute salinity, and density are calculated using the Thermodynamic Equation of Seawater-2010 Matlab Toolbox Version 3.04 [*McDougall and Barker*, 2011].

Aanderaa optodes are mounted on the tail of the gliders to measure concentrations of dissolved oxygen. Following *Hahn et al*. [2014] a two point lab calibration (0% and 100% saturation) of the optodes was carried out on the ship after the deployment. Optodes on gliders exhibit response times between 5 and 175 s [*Bittig et al*., 2014], which result in a hystereses between up and downcasts. These response times were estimated by minimizing the difference of oxygen in up and downcasts. Finally, shipboard CTD profiles close to the glider measurements were used to determine and remove offsets in the final temperature, salinity, and oxygen measurements. The corrected sensor data were gridded on a 1 dbar vertical grid. The gliders have maximum diving depths between 200 and 735 m (Table 1). About one dive (two profiles) was carried out per hour by each glider with lateral resolutions of about 200 m–1 km depending on the maximum diving depth of the individual glider. This resulted in about 10,750 glider CTD profiles within the study area during the 2 month deployment (Table 1).

Gliders can also be used to infer horizontal circulation [*Pietri et al*., 2013, 2014]. The difference between the dead-reckoned and the actual surfacing position of the gliders is used to infer the horizontal depth-averaged velocity between two surfacings, which then is used to reference the relative cross-track geostrophic velocities calculated from the glider-based hydrographic CTD measurements. To reduce the influence of ageostrophic short-term signals (e.g., tides and internal waves), the density field and the depth-averaged velocities have been smoothed prior to calculating the geostrophic shear by a simple rectangular window of 25 km similar to *Pietri et al*. [2013, 2014].

The horizontal circulation was measured by two vessel mounted acoustic Doppler current profilers (vmADCPs) during both cruises M92 and M93. The 38 and 75 kHz ocean surveyor ADCPs (Teledyne RD Instruments) cover depth ranges between 17–800 and 11–245 m, respectively. The standard bin size of the ADCPs was set to 16 m for the 38 kHz ADCP and to 8 m for the 75 kHz, and the ping rates for both instruments were 2–3 s. On the shelf, referred here to water depths shallower than 200 m, the 75 kHz ADCP was occasionally set to 4 m bins to achieve a higher vertical resolution. A comparison of the vmADCP velocity measurements and the glider-based estimates of the geostrophic flow within the PCUC between 10 and 15 January is shown in Figure 2. In both estimates, the PCUC core has a speed of $\sim$0.25 m/s with the core being located between 100 and 150 m depth about 70 km away from the coast. Differences between the two estimates are most pronounced close to the surface. The roots-mean-square difference does not exceed 0.05 m/s below 50 m but increases to 0.1 m/s at 25 m depth. This is likely due to ageostrophic processes, which are more important close to the surface. Furthermore, both platforms did not observe the highly variable flow field at exactly the same time.

A lowered SeaBird SBE 9-plus CTD system equipped with two sets of pumped sensors measuring conductivity, temperature, and oxygen at 24 Hz was used during M92/M93. The CTD was mounted on a General Oceanics rosette with 24 bottles (10 L) which were used to take discrete water samples for sensor calibration and biogeochemical parameters. Salinity samples were measured on board with a Guildline Autosal 8 model 8400B salinometer to calibrate the sensor-based salinity measurements. The calibrated absolute salinity measurements have an accuracy of 0.002 g/kg. The CTD oxygen sensor was calibrated by a combined approach using Winkler titration of discrete water samples obtained from the rosette [*Winkler*, 1888; *Grasshoff et al*., 1983] and STOX (Switchable Trace amount OXygen) sensor measurements at low oxygen concentrations [*Revsbech et al*., 2009; *Kalvelage et al*., 2013]. Note that the classical Winkler titration method is not reliable at oxygen concentrations found in the Peruvian OMZ core and results in too high oxygen

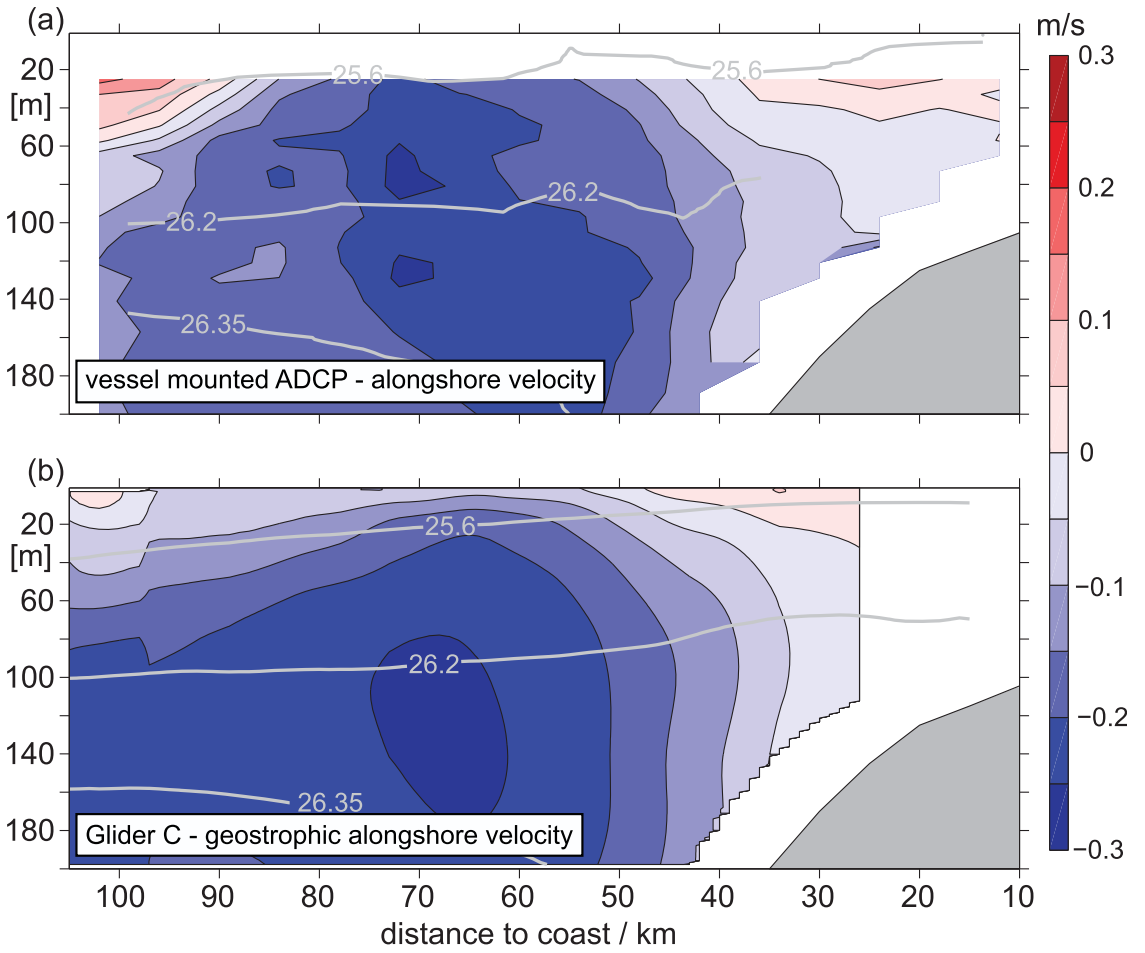

Figure 2. The poleward flow within the Peru-Chile Undercurrent across 12°30′S as observed by the vessel-mounted ADCP and glider C between 10 and 15 January. (top) The alongshore velocity observed by vmADCP measurements and (bottom) geostrophic velocity calculated from glider-based hydrography measurements and referenced by the depth-averaged velocities computed from the vehicle displacement between two dives. Positive/negative velocities correspond to equatorward/poleward (into/out of the page) flow. The black contours have a spacing of 0.05 m/s. Isopycnals are denoted by grey lines.

estimates. To minimize this bias we only used Winkler samples showing oxygen concentrations >20 μmol/kg. The STOX sensor shows oxygen concentrations of about 0.01–0.05 μmol/kg in the OMZ core, which are used to calibrate the CTD oxygen sensor at these depths and resulted in an overall accuracy of the CTD oxygen data of about 1 μmol/kg. Nutrient concentrations were determined onboard the ship by autoanalyzer (Quaatro from Seal Analytical) using standard photometric methods [*Grasshoff et al*., 1983].

For this study, data from two moorings, subsequently referred to as M1 and M2, are analyzed (see blue squares in Figure 1b). They were deployed during M92 in January 2013 on the continental slope off Peru at 700 and 1700 m water depth 12°30.8′S, 77°34.8′W and 12°40.0′S, 77°48.9′W, respectively. Both moorings were recovered during M93 at the end of February 2013. M1 was equipped with an upward looking ADCP (RDI, 300 kHz) at 123 m depth which measured the horizontal velocity every minute in 4 m bins over the depth range of 17–117 m. M2 was equipped with an upward looking ADCP (long ranger RDI, 75 kHz) at 328 m depth measuring the horizontal velocity every 3 min in 4 m bins between 55 and 300 m.

3. Results

3.1. Oceanographic Setting

Being typical for the summer season, moderate southeasterly winds were observed during the two cruises within the study area. Close to the coast ($<$50 km) generally weak winds of 5 m/s in the mean (often below 1 m/s) were measured. Further offshore the winds increased to 9 m/s at 150 km distance from the coast

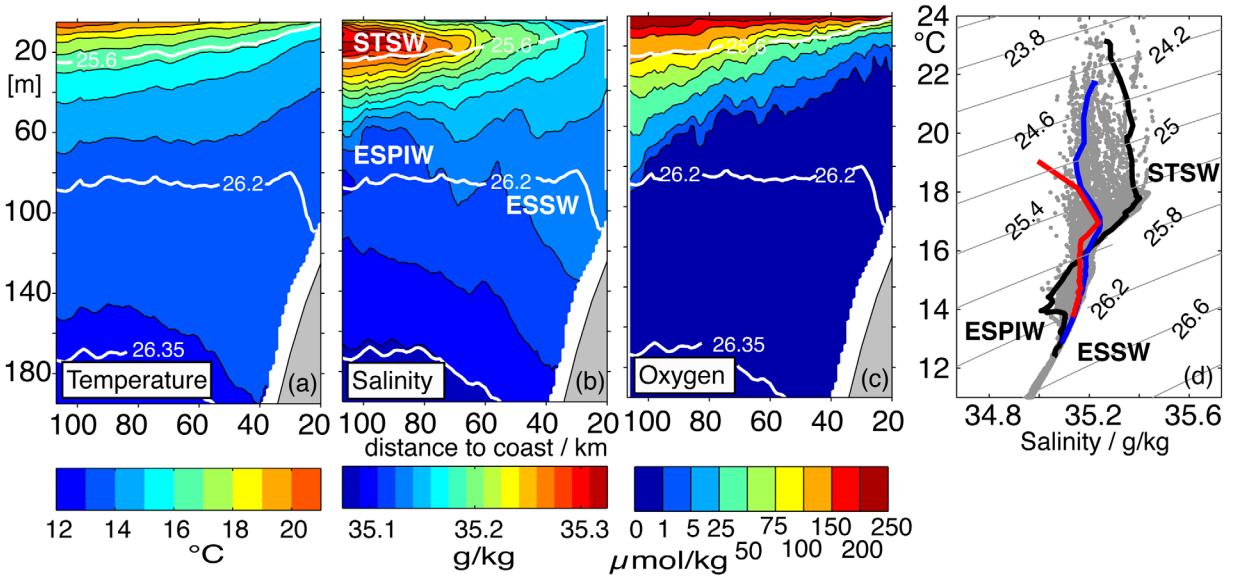

Figure 3. (a) Mean conservative temperature in °C, (b) absolute salinity in g/kg, and (c) dissolved oxygen (nonlinear color scale) in μmol/kg distributions near 12°30′S between 10 January and 27 February measured by glider C (Figure 1b). Twelve transects have been horizontally smoothed on a 1 km grid by a rectangular 5 km running mean window and subsequently temporally averaged. Isopycnals are contoured in white. (d) All CTD measurements are shown with grey dots in the T/S diagram. The following water masses: Subtropical Surface Water (STSW), Eastern South Pacific Intermediate Water (ESPIW), and Equatorial Subsurface Water (ESSW) are marked in Figures 3b and 3d. Three representative glider profiles (offshore (black, blue) and upper shelf (red)) are overlaid and can be found in the transect in Figure 10h.

(not shown). At the beginning of our measurement campaign, from 10–15 January 2013, a strong PCUC with maximum poleward alongshore velocities of ~0.25 m/s between 100 and 200 m depth was observed extending from the upper continental slope at 400 m water depth to about 80 km offshore (Figure 2). A near-surface current is seen to be most pronounced around 90–100 km offshore with equatorward velocities of up to 0.1 m/s, possibly associated with the Peru Coastal Current (Figure 2). On the shelf, at water depths shallower than 150 m, the flow is southwestward with velocities lower than 0.1 m/s.

During January and February, different water masses are encountered along the main transect near 12°30′S off Peru (glider C, Figures 1b and 3). Near-surface temperatures reach maximum values of 21.5°C at 100 km offshore and decrease to about 17°C toward the coast. As is typical for the summer season in this region, the thermocline is very shallow and no surface mixed layer is discernible (Figure 3a). About 80 km offshore, a subsurface salinity maximum of about 35.3 g/kg is found within the thermocline at 20 m depth (Figure 3b). The salinity maximum can be associated with Subtropical Surface Water (STSW, Figures 3b and 3d). This is a highly oxygenated water mass found both in the mixed layer and the upper thermocline off Peru originating from the eastern flank of the subtropical gyre [*Wyrtki*, 1967; *Karstensen and Quadfasel*, 2002; *Fiedler and Talley*, 2006; *Silva et al.*, 2009]. Below the thermocline, the relatively salty and low-oxygen Equatorial Subsurface Water resides (ESSW, Figures 3b and 3d), which is transported southward in the PCUC [*Gunther*, 1936; *Fonseca*, 1989; *Silva et al.*, 2009; *Montes et al.*, 2010]. In the same density range as the ESSW but offshore, the Eastern South Pacific Intermediate Water (ESPIW, Figure 3d) is present. The ESPIW originates off southern Chile and is characterized by a distinct salinity minimum in the T/S diagram at densities of about $\sigma_\theta = 26\,\mathrm{kg/m^3}$ [*Schneider et al.*, 2003]. It has also been referred to as Shallow Salinity Minimum Water [*Karstensen*, 2004]. For simplicity, we shall refer to STSW and ESPIW in most cases just as high and low-salinity water masses, respectively. The oxygen concentrations are highest close to the surface with mean values of up to 240 μmol/kg (Figure 3c). They decrease rapidly with depth and are <1 μmol/kg below ~30 m on the shelf and at ~80 m further offshore, respectively.

3.2. Eddy Formation

The near-coastal horizontal circulation off Peru near 12°30′S exhibited pronounced changes in January and February 2013 due to the formation of a subsurface anticyclonic eddy. The chronology of the eddy formation is subsequently described. While a persistent PCUC was observed until 19 January, the current core moved offshore during the following week (Figure 4). Concurrently, an equatorward flow appeared along

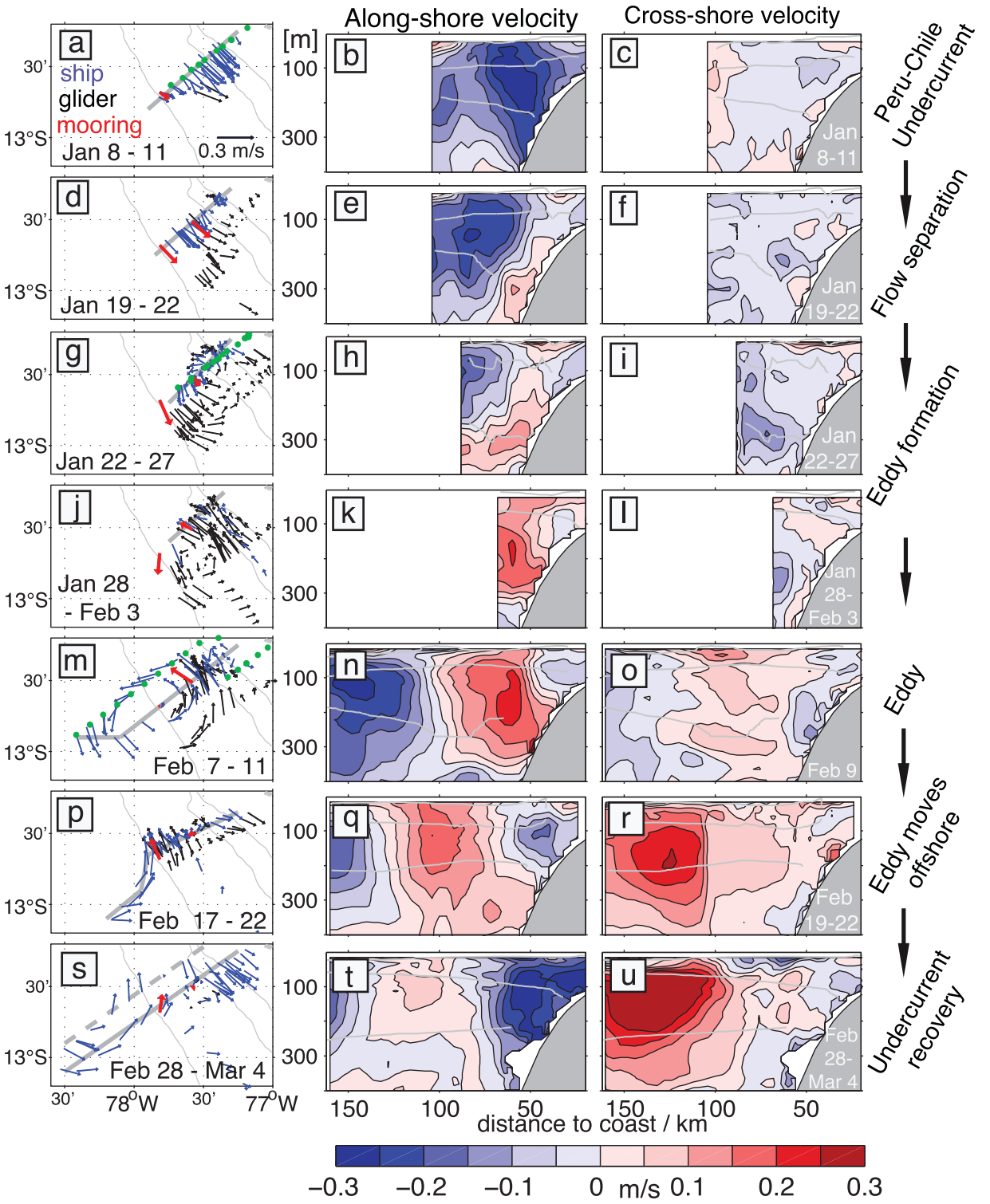

Figure 4. (left column) The depth-averaged horizontal circulation for eight selected periods based on vmADCP (blue), moored ADCP (red), and glider drift-inferred velocities (black). The 200, 400, and 2000 m isobath is contoured in black. The temporal evolution of the (middle column) alongshore (positive/negative = equatorward/poleward = into/out of the page) and (right column) crossshore (positive/negative = onshore/offshore = to the left/right) velocity components (vmADCP) along the grey transects (left column). Isopycnals (25.6, 26.2, and 26.4) are contoured in grey. The green dots in the left column indicate the position of the nutrient measurements shown in Figure 14.

the upper continental slope between 250 and 350 m depth (Figures 4e, 4h, and 4k). Small-scale velocity fluctuations and a first eddy-like structure were observed between 22 and 27 January (Figure 4g). It developed into a coherent eddy centered at around 77°30'W, 12°45'S between 28 and 3 February (Figure 4j).

A week later, between 7 and 11 February, the eddy center was located directly at the M2 mooring (Figure 4m), where velocities close to zero were measured during this period. A complete vmADCP-based velocity transect through the eddy was obtained on 9 February (Figure 4n). Maximum velocities of 0.25 m/s were found between 100 and 200 m depth. The eddy diameter, here defined as the distance between the two velocity maxima, was about 90 km (Figure 4n). Strong acrossshore velocities were found during and after the eddy formation at and offshore of the continental slope (Figures 4g, 4j, and 4m). At the southern eddy periphery, onshore velocities advected offshore water toward the continental slope with velocities near 0.25 m/s (Figures 4r and 4u). North of the eddy, coastal waters were advected offshore (Figure 4m). These eddy-induced crossshore velocities might be crucial, as they potentially provide an important coastal open ocean exchange mechanism.

On the upper continental slope, poleward velocities of about 0.1 m/s were again observed in mid-February and subsequently increased to values of more than 0.2 m/s by early March (Figure 4t). This is close to the initial state of the PCUC encountered in early January (Figure 4b).

In mid-February, the eastern eddy edge was still clearly visible at around 78°W (Figure 4p). The center had moved to about 12°45′S and 78°10′W, covering a distance of 40 km in 6 days. This translates into a westward drift of about 0.08 m/s. In early March (i.e., at the end of the study period), velocity measurements close to the eddy core were carried out again (Figure 4s).

Sea surface height anomaly data from satellite observations (AVISO) provided no reliable means to track the eddy path during and after the field campaign. In fact, during the formation of the eddy close to the continental slope, the geostrophic surface velocity field strongly disagreed with our in situ velocity measurements. This might be explained first by known problems of altimetry products close to the coast [*Vignudelli et al*., 2011] and second the fact that the rapid changes of the flow field during the formation process could not be captured by the sparse altimetry measurements. However, a clear isolated sea level anomaly signal was also not detectable offshore by the end of the study period. Such a signal is required to track the eddy path by established tracking algorithms [*Okubo*, 1970; *Weiss*, 1991]. The subsurface eddy is probably not seen by altimetry because of its small size and its weak or sometimes absent surface velocities. The uppermost vmADCP measurement deviates by up to 0.25 m/s from the subsurface velocity (e.g., Figure 4n). Furthermore, the eddy with a radius of 45 km is of relative small size when considering the mapping scale of 250 km used by AVISO in the tropics [*Ducet et al*., 2000]. Thus, it is an important finding that energetic subsurface eddies exist off Peru, which are not visible in altimetry products. Nevertheless, we expect that the eddy propagated further westward after our study period as we were able to observe its strong potential vorticity (*PV*, see below) anomaly in the eddy core right until the end of our observations (Figure 5t). This indicates that the eddy was still intact at the point.

3.3. Potential Vorticity and Eddy Generation Mechanism

Subsurface anticyclones similar to the one observed here are often characterized by very low *PV* and this is thought to play an important role during eddy formation [*McWilliams*, 1985; *D'Asaro*, 1988; *Molemaker et al*., 2015]. Ertel's *PV* is defined as $PV=\omega_a \cdot \nabla b$, where $\omega_a=(f\mathbf{k}+\nabla\times\mathbf{u})$ is the absolute vorticity with f being the Coriolis parameter, $\mathbf{k}$ the vertical unit vector, and $\mathbf{u}$ the velocity vector [*Gill*, 1982]. The buoyancy is given by $b=-g\rho/\rho_0$, where g is the gravitational acceleration, ρ the potential density, and ρ_0 a reference density. *PV* is conserved in the absence of tracer and/or momentum mixing and is thus an ideal to identify and track water masses.

We approximate *PV* by the part associated with the stratification ($N^2=\partial b/\partial z$) and the vertical component of the absolute vorticity ($\zeta_{abs}=f+\zeta_z$), where $\zeta_z=\partial v/\partial x-\partial u/\partial y$ is the vertical component of the relative vorticity. In cases of weak lateral buoyancy gradients as observed here and below the mixed layer, this is usually a good approximation. Only one component of the vertical relative vorticity ($\partial v/\partial x$) is calculated, as we are only able to compute the spatial derivative of the alongshore velocity from the data. Thus, here we compute $PV \approx N^2(f+\partial v/\partial x)$, where v is the alongshore velocity and x points toward the coast. Given that observed *PV* structure is largely dominated by distribution of N^2 (Figure 5, third and fourth column) the omittance of one term in the relative vorticity has a minor effect. Note that f is negative in the southern hemisphere and therefore negative *PV* values reflect stable conditions in respect to symmetric instability [*Hoskins*, 1974; *Thomas et al*., 2013]. Thus, we multiply the *PV* with the local Coriolis parameter f to obtain

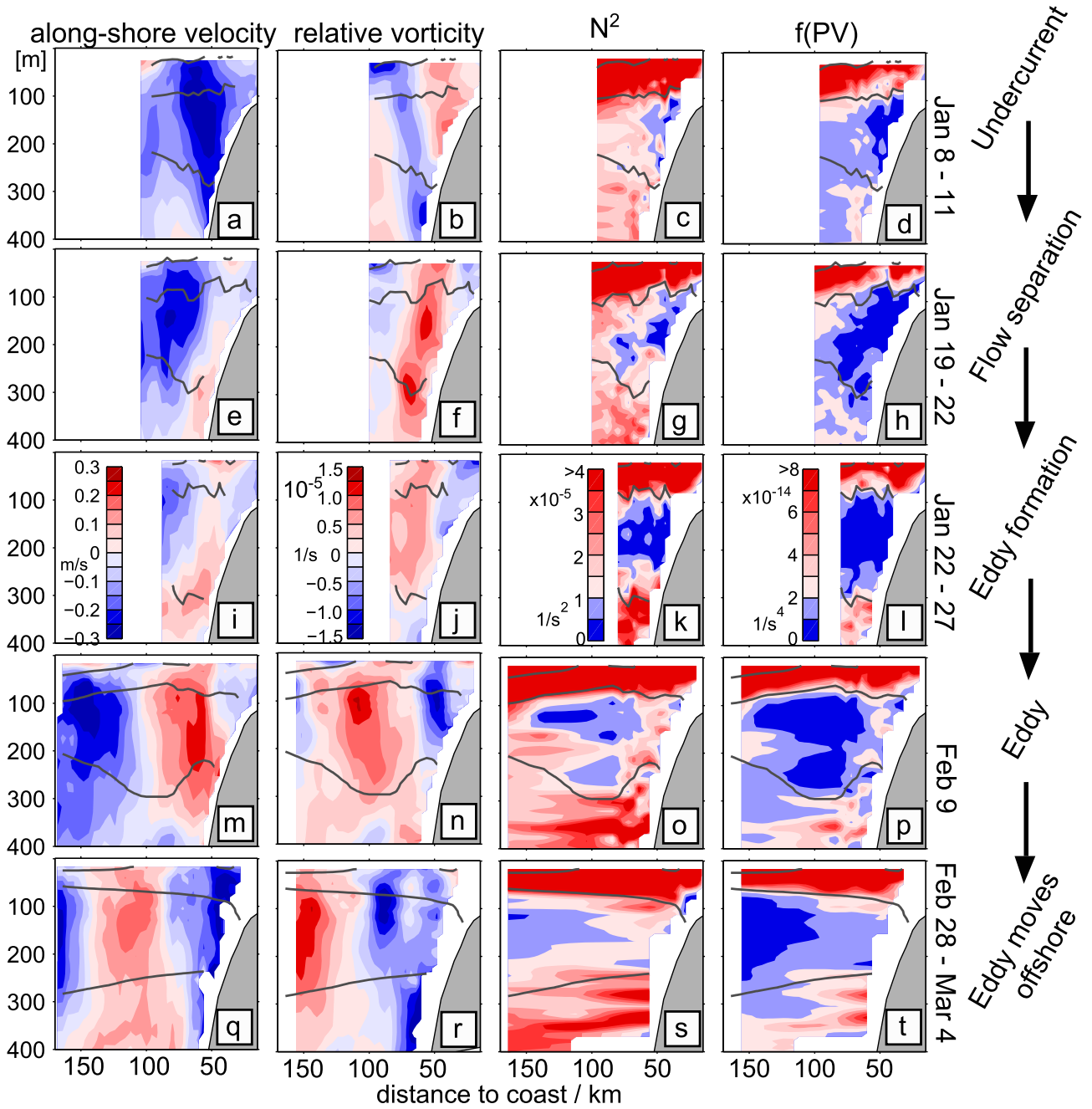

Figure 5. (first column) The alongshore velocity (vmADPC) in m/s where positive/negative values correspond to equatorward/poleward (into/out of the page) flow. (second column) The two-dimensional relative vertical vorticity ($\zeta^z = \partial v/\partial x$, where v is the alongshore velocity and x points toward the coast). (third column) The stratification ($N^2 = -(g/\rho_0) \cdot (\partial\rho/\partial z) - (g/c_s)^2$, with g being the gravitational acceleration, ρ the potential density, ρ_0 a reference density, and c_s the sound speed). (fourth column) The *PV* times f, with $PV = N^2(f + \partial v/\partial x)$. Isopycnals (25.6, 26.2, and 26.45) are contoured in grey. All transects go along the main transects as marked with grey in the left column of Figure 4. Only the last transect is slightly further north of the main transect to be closer to the eddy core (dashed grey line in Figure 4s).

positive *PV* values, which allows an easier comparison with northern hemisphere estimates. For simplicity, we shall refer to *fPV* as *PV* in the following.

At the beginning of our observations, positive (negative) relative vorticity (Figure 5b) is found onshore (offshore) of the PCUC core and the stratification is weakest near the bottom at the continental slope (Figure 5c). The combination of positive relative vorticity and weak stratification results in a band of *PV* close to zero in the bottom boundary layer at 100–250 m depth (Figure 5d). The negative vorticity band further offshore acts in the opposite direction and increases *PV*. When the eddy starts to form end of January, both the band of

positive relative vorticity and the low stratification move further offshore (Figures 5f and 5g). Consequently, the low *PV* patch increases in size during the ongoing eddy formation. At this point it is no longer restricted to the area close to the topography (Figure 5l). When the eddy has finally separated from the topography, minimum *PV* values are found in its core in a depth range between 100 and 300 m (Figure 5p). These *PV* values agree well with the observed values close to the bottom on the continental slope prior to the eddy formation. The relative vorticity increases toward the eddy core and maximum values around 1.2×10^{-5} 1/s (0.38*f*) are found between 100 and 150 m depth. Note that we only compute the component of the relative vorticity associated with $\partial v/\partial x$ and thus the full relative vorticity in the eddy core should be up to factor of 2 larger (around 0.75f) assuming solid body rotation. This is in good agreement with relative vorticity values found in the high-resolution model simulation of *Molemaker et al.* [2015].

About 3–4 weeks after the first transect through the fully developed eddy (Figure 5m), another transect was obtained toward the end of the observations (Figures 4s and 5q). It shows that the low *PV* within the eddy core has moved offshore as a result of the eddy's westward propagation.

Given that the absolute vertical vorticity is dominated by *f*, pure adiabatic vortex stretching (e.g., due to unforced flow instabilities) will result in increased cyclonic vorticity. It thus cannot explain the low stratification in the core of the observed eddy, because the relative vorticity there is anticyclonic. Thus, the low stratification must have been caused by diapycnal mixing prior to the eddy formation near the surface [*McWilliams*, 1985] or near boundaries [*D'Asaro*, 1988]. The latter case is of importance here, as the eddy core waters originate from the equatorial region and moved within the PCUC along the continental slope before they end up in the eddy. As our observations were made in the summer season when atmospheric cooling events do not occur, it cannot explain the reduction of the *PV* locally. As subsurface eddies tend to be anticyclones the classical baroclinic and barotropic instability mechanisms alone cannot explain their formation, because such eddies have no preferred symmetry [*McWilliams*, 1985; *Molemaker et al.*, 2015]. In agreement, off Peru, a skewness toward anticyclonic vorticity is found at depth [*Colas et al.*, 2012]. A plausible explanation for this might be the geometry of the PCUC flowing poleward along the continental slope, which results in anticyclonic vorticity between the PCUC core and topography.

D'Asaro [1988] and *Molemaker et al.* [2015] point out the importance of sharp topographic variations for the separation of the low *PV* boundary water from the topography. This will be investigated in the following. Indeed, we observed the first appearance of an eddy-like structure just downstream of an abrupt change in the curvature of the isopleths (Figures 4g and 6). Thus, we hypothesize that flow separation is responsible for the eddy formation. This is supported by our observations as will be shown in the following. First, the PCUC core flows along the 400 m isobath (Figure 4b) which exhibits two sharp bends in the study area (Figure 6). The second bend is of relevance here as it can force the PCUC to separate. In this region, the offshore displacement of the PCUC is seen in the velocity measurements prior to the eddy formation (Figures 4d–4i). Second, the initial disturbances developing into an eddy-like structure (Figure 4d) are found about 15 km downstream from the topographic bend shown in Figure 6. Black crosses in Figure 6 show the position of the eddy center directly after its formation. The eddy is clearly formed downstream of the second topographic bend and then propagates westward.

Marshall and Tansley [2001] propose that the separation of a barotropic boundary current at a vertical sidewall takes place when $r < L=(U/\beta)^{1/2}$. Here *r* represents the radius of curvature of the coastline, which is 7.5 km at the location shown in Figure 6. *U* is the boundary current speed, here 0.25 m/s and β is the planetary vorticity gradient in the downstream direction (1.8×10^{-11} 1/s). This yields a length scale *L* of about 120 km. As $r \ll L$, this suggests that flow separation would occur for a case with a vertical sidewall. However, given that the PCUC flows along the topographic slope we propose to use $\beta_{eff}=fs/H$, instead of the usual β, where *f* is the Coriolis parameter, $s=((\partial H/\partial x)^2+(\partial H/\partial y)^2)^{1/2}$ is the bottom slope, and *H* the depth scale of the boundary current, in order to account for the topographic beta effect. Following the early work of *Pedlosky* [1979] on the inertial boundary layer problem, *Kinsella et al.* [1987] used the same formula to investigate the interaction of the Labrador current with the topography of a canyon. With *H* set to 400 m, the topographic beta is around 2.5×10^{-9} 1/s near this bend and decreases further downstream. This implies that β_{eff} is about 2 orders of magnitudes larger than β and thus probably more important for the dynamics of the PCUC. Using β_{eff} near the bend instead of β yields $L = 10$ km, which is still larger than the radius of the bend and suggests flow separation. However, given that the separation criteria of *Marshall*

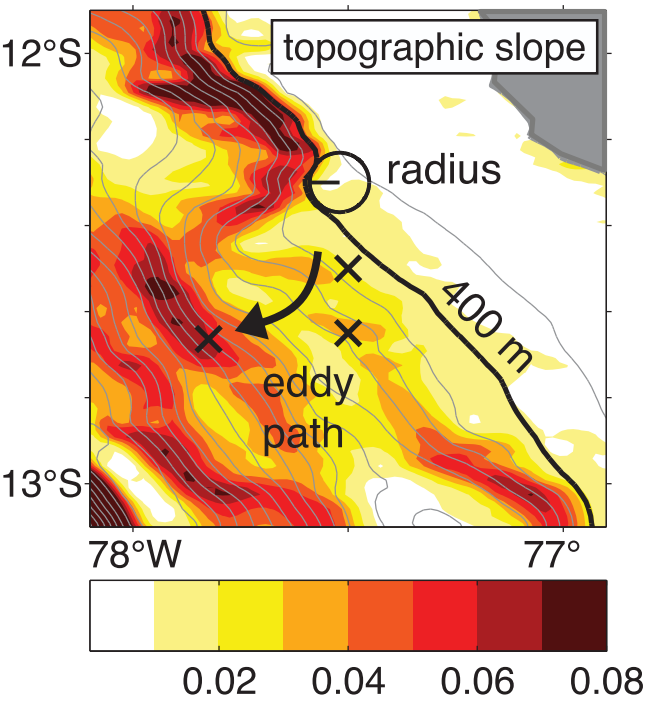

Figure 6. The bottom slope $s=((\partial H/\partial x)^2+(\partial H/\partial y)^2)^{1/2}$ (color coded) and water depth (grey contours, 200 m interval) are shown. The radius of the topographic curvature and the 400 m isobath are shown in black. The three black crosses indicate the position of the eddy center during three different time periods (22–27 January, 28 January to 3 February, and 7–11 February).

and Tansley [2001] does not account for topographic effects, further research is required to validate our proposed modification.

Given that the swirl velocity and both the relative vorticity and *PV* anomalies did not lose their strengths, even toward the end of our study period, we suspect that the eddy continued to propagates further westward into the open ocean. The pronounced *PV* anomaly first would have had to dissipate before the eddy may decay. However, as we are not able to track the eddy via altimetry, we can only speculate about its further propagation and life cycle.

3.4. Impact of the Horizontal Circulation on the Distributions of Salinity and Oxygen

Pronounced variability in salinity and oxygen is observed in the upper ocean along the continental margin off Peru during January and February 2013. The extensive hydrographic data set allows a detailed description of the evolution of salinity and oxygen characteristics prior, during and after the eddy formation. Three processes are of major importance for the distributions of salinity and oxygen in the study area during the observational period: advection along isopycnals in a vertically sheared flow, mesoscale stirring, and eddy-driven ventilation. Each process will be discussed in a separate subsection. A summary schematic is given in Figure 7 to guide the reader through the complex data and should be seen as a hypothesis at this point, which is supported by our observations in the later sections. The schematic is based on both the observed distributions of salinity and oxygen on selected isopycnals (Figure 8) and the three-dimensional fields (Figure 9). The analysis focuses mainly on two water bodies characterized by distinct salinity and oxygen concentrations (Figures 8 and 9). As our first measurements were made in early January, we cannot say much about the history of these water mass patches prior to this period, besides their broad formation area (see section 3.1). In section 3.4.1, we describe the formation of isolated oxygen patches in the OMZ. We suggest that they are formed prior to the eddy formation by advection along isopycnals in the upper part of the PCUC that exhibits a pronounced vertical shear of the horizontal flow (Figures 7a–7d). During the eddy formation, the two water bodies are thought to be found south of the study area (Figures 7e and 7f). After the eddy formation, the near-coastal flow reverses toward northward flow and the water bodies are advected into the study area again (Figures 7g and 7h). In section 3.4.2, we investigate the role of mesoscale stirring for the generation of small-scale salinity and oxygen structures by describing the formation of such salinity structures at the eddy edge in detail (Figures 7g and 7h). Finally, in section 3.4.3, we investigate the role of the eddy for the ventilation of the near-coastal OMZ, which is indicated by a deepening of the oxycline in Figure 7h.

3.4.1. Formation of Isolated Oxygen Patches by Advection Along Isopycnals in a Vertically Sheared Flow Prior to the Eddy Formation

When tracers are advected along isopycnals in a vertically sheared flow, they will separate horizontally due to the different speeds at different depths. Given that along-isopycnal salinity and oxygen gradients are observed in regions of vertically sheared flow, it can be expected that this separation process might contribute to the observed distributions of salinity and oxygen.

The temporal evolution of the alongshore geostrophic velocity and the vertical distributions of salinity and oxygen along the main transect near 12°30′S (glider C) between 10 January and 27 February is shown in

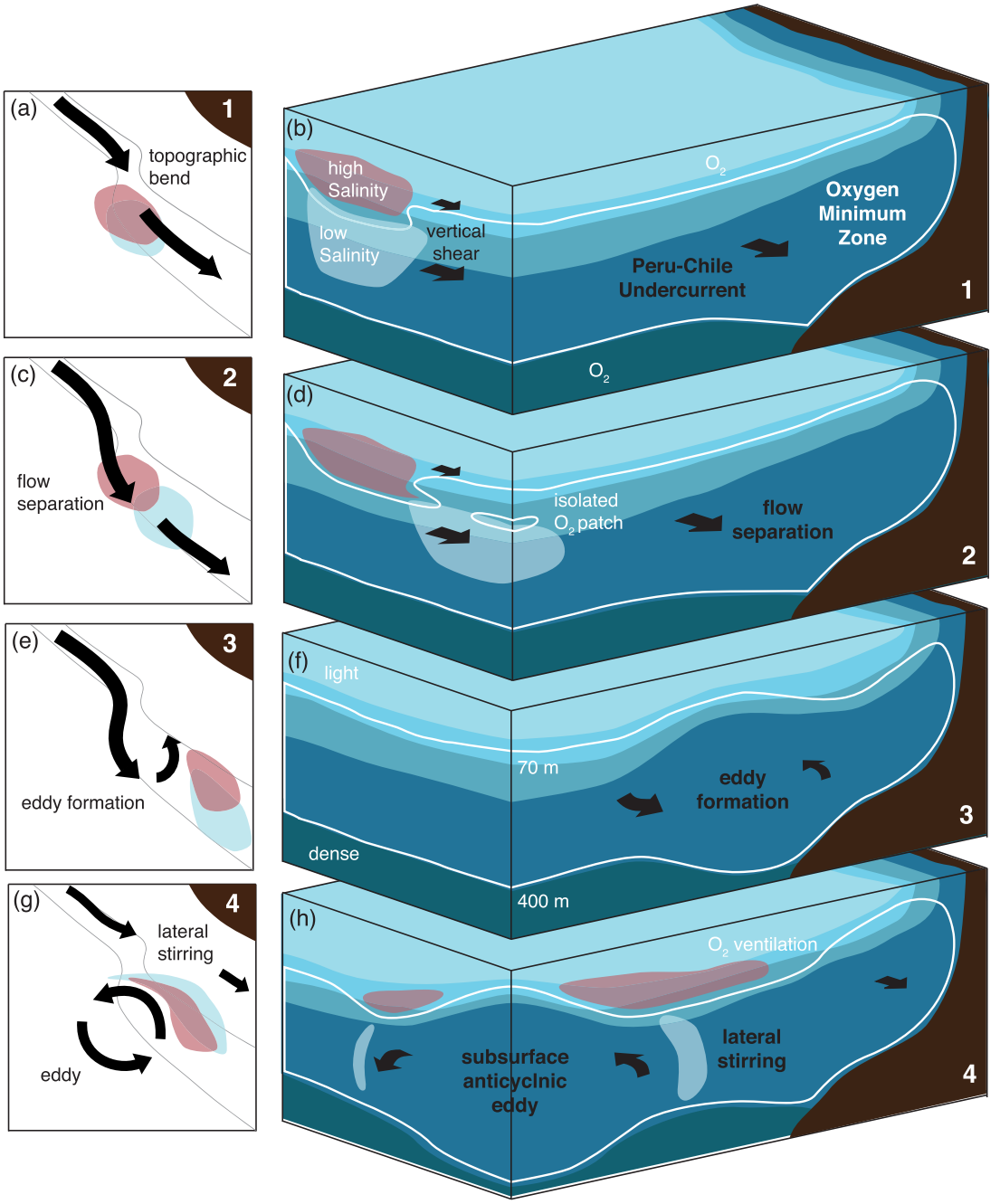

Figure 7. Schematic showing the formation history of the subsurface anticyclonic eddy (left column) as horizontal maps and (right column) as three-dimensional views. We highlight the impact of the circulation on the salinity and oxygen distributions, including (a–d) the formation of isolated oxygen patches by advection along isopycnals in a vertically sheared flow and (g, h) the formation of low-salinity structures at the eddy periphery and the ventilation of the near-coastal oxygen minimum zone both by lateral stirring. The horizontal circulation is represented with black arrows. Two grey lines in the left column represent topography contours. The high and low-salinity water bodies are shown in red and light blue, respectively. The oxycline is represented by the white line and the density stratification is shown by different shades of blue (from dark blue/dense to light blue/light).

Figure 10. During the first three transects prior to the eddy formation, a well-defined PCUC is observed and low-salinity water is present below 50 m and 70–100 km offshore (Figures 10b, 10e, and 10h). In the thermocline above this low-salinity water, a well-oxygenated water mass with much higher salinities is observed (Figures 10e, 10f, 11a, and 11c). Until around 22 January, the horizontal circulation is dominated by the along-shelf flow and both water bodies are transported poleward by the PCUC with a speed of 0.15–0.25 m/s (Figure 4). The low-salinity water is advected southward at higher speeds than the high-salinity

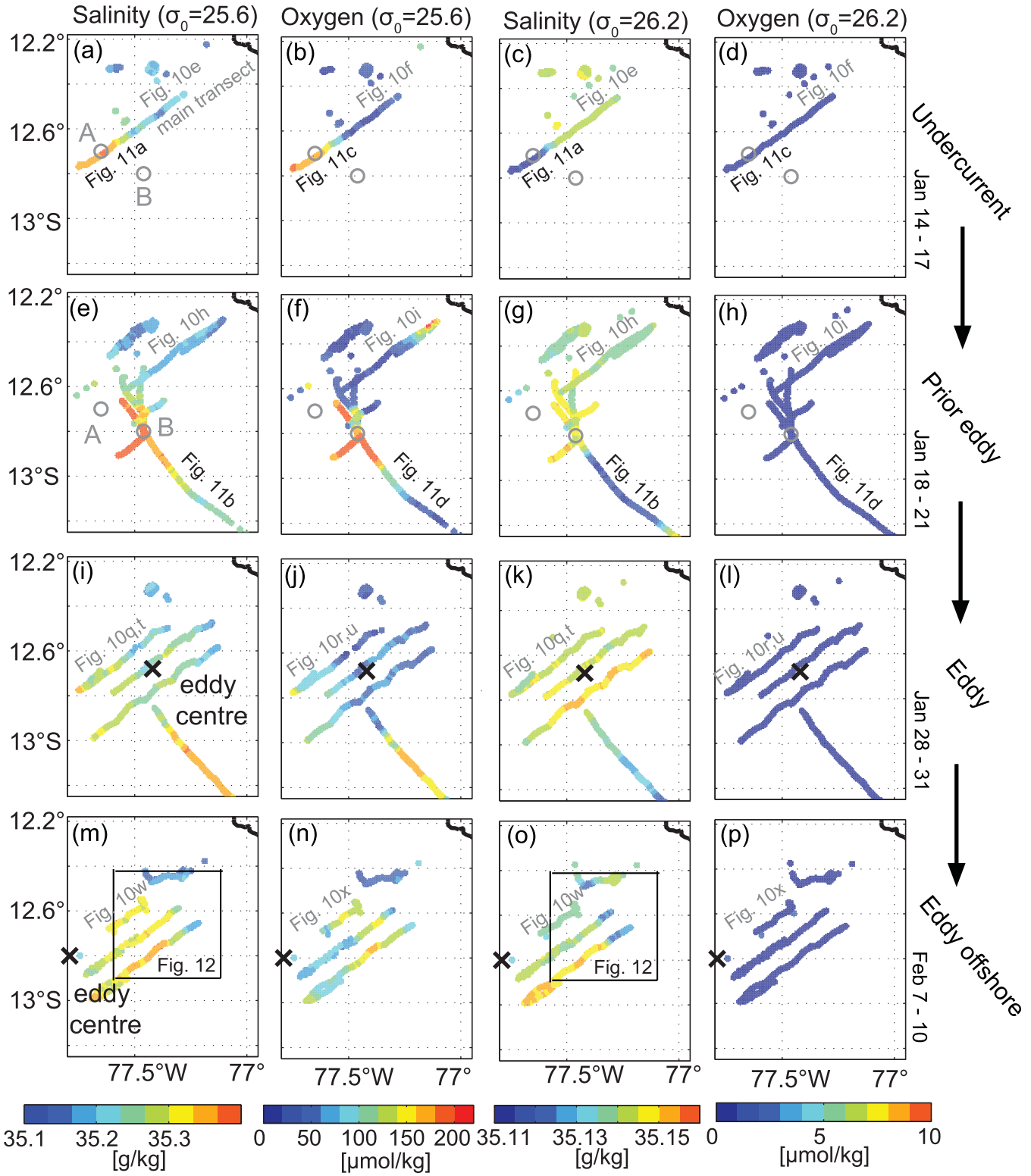

Figure 8. Absolute salinity (g/kg) in the σ_0 range of (first column) 25.61–25.63 kg/m^3 and (third column) 26.19–26.2 kg/m^3 and corresponding oxygen concentrations (μmol/kg), respectively, (second and fourth column) at four different time spans (prior to the eddy formation (first and second rows), just after the eddy formation (third row), and about a week after the eddy formation (fourth row)). All glider and CTD salinity and oxygen data have been gridded prior plotting using a simple Gaussian mapping algorithm with a small influence radius of 1 km (1.5 km cutoff radius).

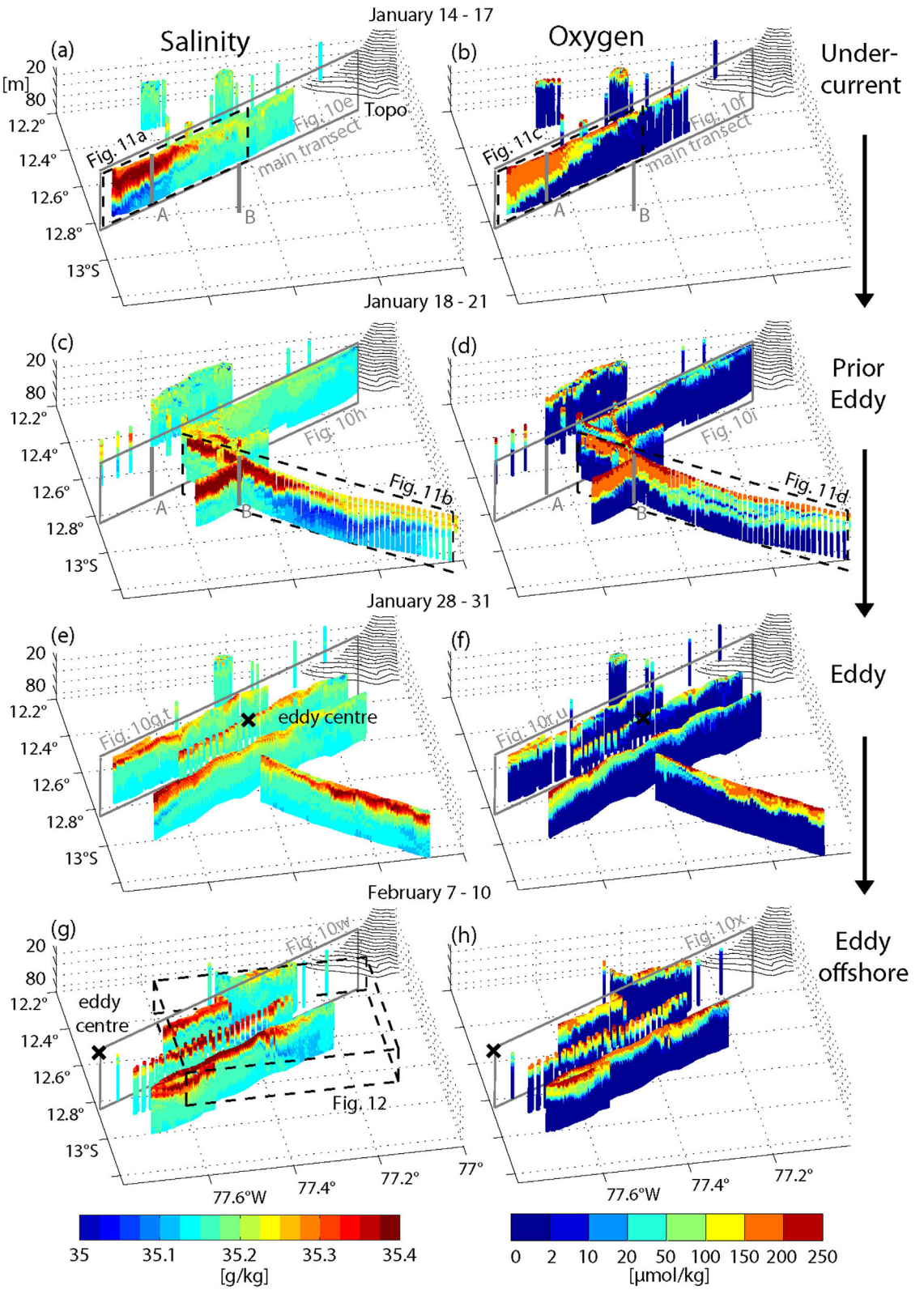

Figure 9. Snapshots of three-dimensional (left) absolute salinity (g/kg) and (right) oxygen concentrations (μmol/kg) fields around 12°45′S and 77°24′W between 10 and 90 m at four chosen time spans ((a–d) prior to the eddy formation, (e, f) just after the eddy formation, and (g, h) about a week after the eddy formation). The main transect (Figure 10, glider C) is marked by gray boxes. The dashed black boxes mark the transects shown in Figure 11, and the three-dimensional salinity field at the eddy edge (Figure 12). The points A and B (vertical gray lines) are discussed in section 3.4.1.

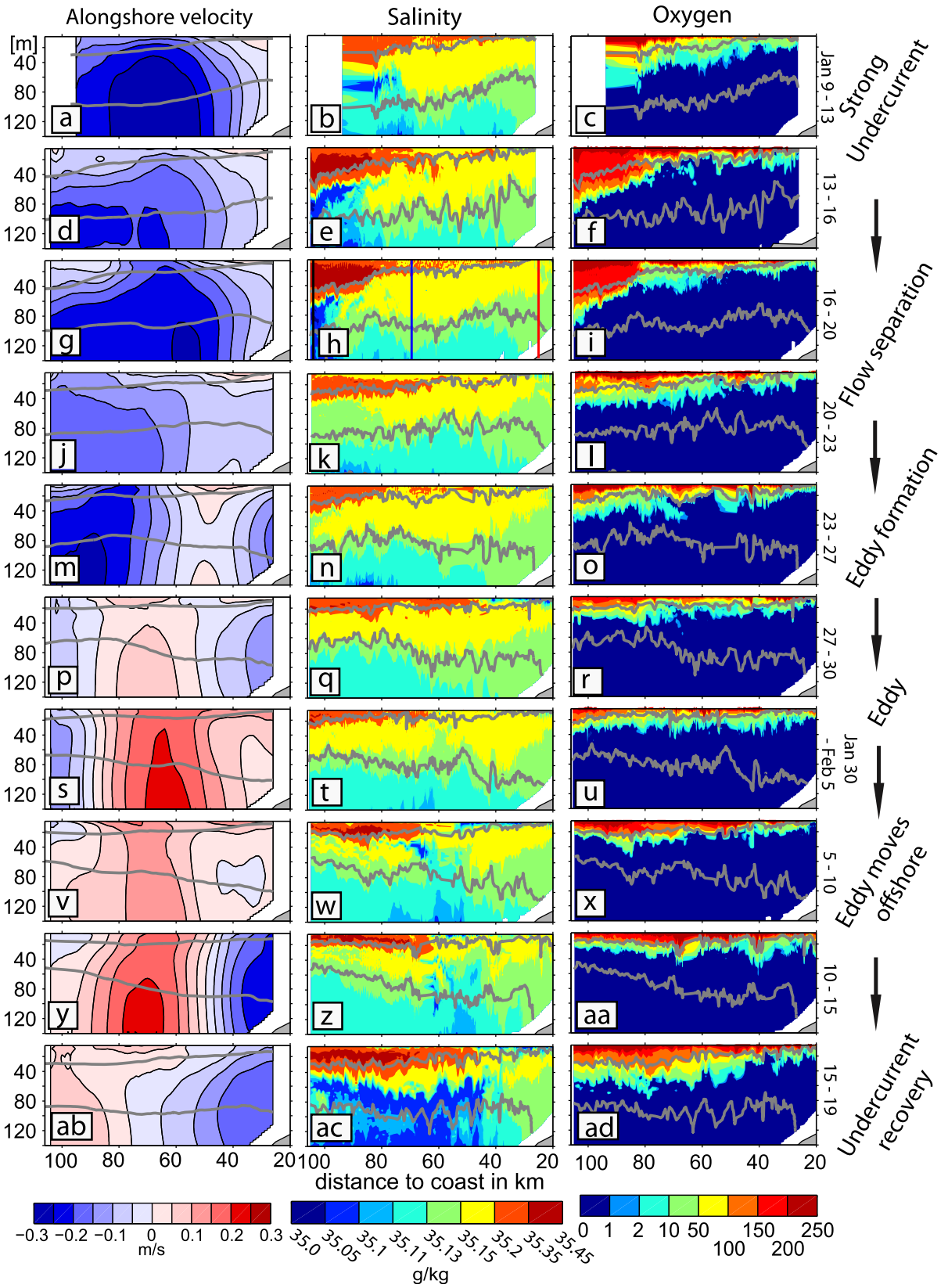

Figure 10. (left column) Alongshore geostrophic velocity (positive/negative = equatorward/poleward = into/out of the page) in m/s, (middle column) vertical distributions of salinity in g/kg, and (right column) oxygen in μmol/kg along 12°30′S as measured by glider C between 10 January and 23 February 2013. The geostrophic velocity is color-coded (0.05 m/s interval) and isopycnals (25.6 and 26.2 kg/m^3) are contoured in grey.

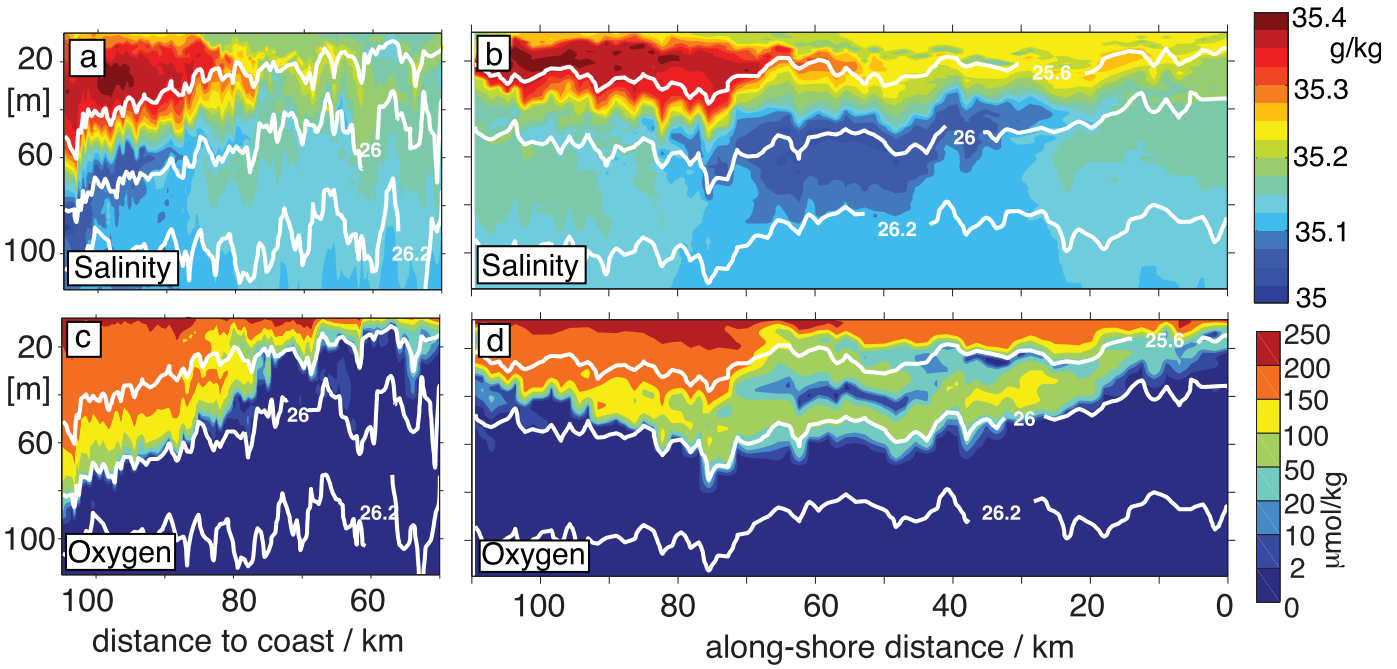

Figure 11. (top row) Absolute salinity (g/kg) and (bottom row) oxygen concentration (μmol/kg) transects observed by (left column) glider C between 13 and 16 January and (right column) glider G between 17 and 22 January within the Peru-Chile Undercurrent prior to the eddy formation. Isopycnals are shown by white lines. Please note the different orientations of the two transects in space (top = across shelf, bottom = along shelf), as shown with dashed black rectangulars in Figures 9a–9d.

water, as it is closer to the PCUC core. This can be seen in the along-coast transect of glider G, which sampled the same water bodies during their poleward advection along the coast (Figures 8a–8h, 9c, 9d, 11b, and 11d).

In contrast to the salinity distribution, the oxygen distribution is more straightforward to interpret. High oxygen levels of up to 250 μmol/kg are restricted to the uppermost layers, while oxygen concentrations below 80 m rarely exceed 1 μmol/kg. However, at depth shallower than 80 m (or at densities smaller than 26.0 kg/m^3), along-isopycnal gradients of oxygen are present in this region (Figure 3). In the following, we focus on the well-oxygenated water body found near the surface between 80 and 100 km offshore on the main transect between 14 and 18 January (Figures 10f, 10i, and 11c). This water body is of particular interest since it shows strong along-isopycnal oxygen gradients, which are required for eddy-driven along-isopycnal oxygen fluxes (Figures 11c and 11d). Note that the vertical oxygen gradient is not perfectly collocated with the vertical salinity gradient. Hence, the upper part of low-salinity water still shows comparably high oxygen concentrations, which fall below 2 μmol/kg at densities larger than $\sigma_\theta \approx 26\,\mathrm{kg/m^3}$. During the southward advection of these waters, isolated oxygen patches are formed in the depth range between 40 and 60 m south of the main transect (Figures 9d and 11d).

It follows that advection along isopycnals in a vertically sheared flow might explain the separation of the high and low-salinity waters and the formation of the isolated oxygen patches described above. This hypothesis is tested using a simple calculation of linear tracer advection along the slope relying on the observed value for the flow speed and the distributions of salinity and oxygen at two depth levels, namely 30–70 m. This simple setup is inspired by the typical PCUC flow structure showing mainly southward currents in the domain up until 22 January. Based on our measurements, we assume that salinity and oxygen are advected southward along the coast with speeds of 0.15 and 0.25 m/s at a depths of 30 and 70 m, respectively (Figure 10). This translates into a horizontal displacement of 30 km at 30 m depth and 50 km at 70 m depth between point A (Figures 8a–8h and 9a–9d, 12°42′S and 77°39′W, 16 January 06:00) and point B (Figures 8a–8h and 9a–9d, 12°48′S and 77°28′W, 18 January 12:00) over a period of 54 h. This duration corresponds to the time difference between the measurements taken at the two points shown in Figure 9. The distance between the points is ~23 km. Consequently, the saline water mass still is present at point B at around 30 m depth on 18 January 12:00 (Figures 8e and 9c), while larger velocity at 70 m has allowed the

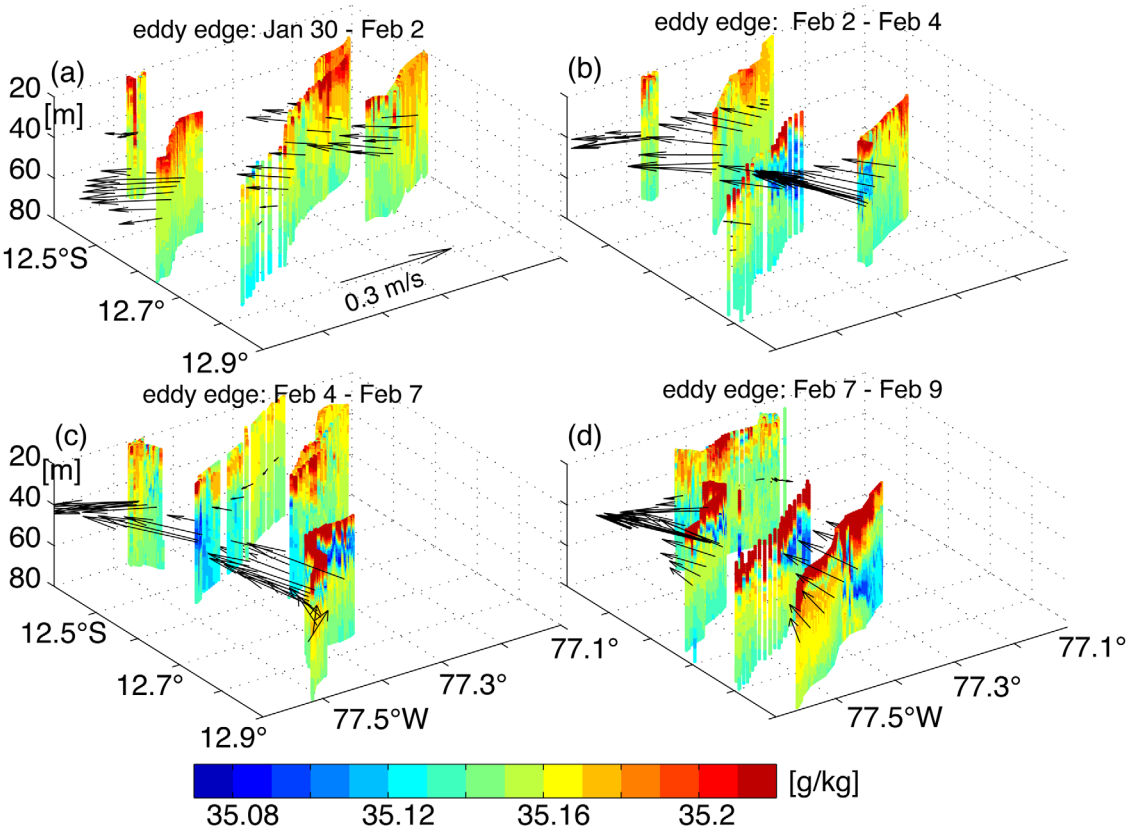

Figure 12. Snapshots of the near-surface (20–80 m) absolute salinity (g/kg) at the inshore eddy edge during four different time periods (of 2.5 days length) between 30 January 18:00 and 9 February 18:00. The depth-averaged velocity is shown by the black arrows. The location of this box is shown in Figure 9g.

advection of the deeper low-salinity water further downstream (Figures 8g and 9c). Our calculation thus supports the assumption of advection along isopycnals in a vertically sheared flow as an explanation for the observed separation of the high and low-salinity water and formation of isolated oxygen patches.

3.4.2. Formation of Small-Scale Salinity and Oxygen Structures by Mesoscale Stirring After the Eddy Formation

Mesoscale stirring of along-isopycnal tracers gradients (e.g., of salinity and oxygen) has to be shown to result in the formation of small-scale tracer structures [*Smith and Ferrari*, 2009]. Our observations show small-scale salinity and oxygen structures in the upper ∼150 and ∼80 m of the water column, respectively (Figure 10, middle and right column). As along-isopycnal salinity and oxygen gradients exist in these depth ranges (Figures 3b and 3c), we propose mesoscale stirring of along-isopycnal salinity and oxygen gradients as the primarily process generating the structures. In the following, we describe the formation of small-scale salinity structures at the eddy periphery as an example of mesoscale stirring (Figures 10w, 10z, and 12).

No distinct salinity and oxygen patches are found along the main transect covered by glider C cutting through the newly formed eddy (Figures 10t and 10u). Rather, the eddy core exhibits homogeneous temperature (12–14°C), salinity (35–35.15 g/kg), and oxygen (<1 μmol/kg) fields. This is confirmed by the three-dimensional salinity and oxygen fields shown in Figures 9e and 9f. During the subsequent offshore propagation of the eddy, small-scale salinity features appear at its onshore edge between 50 and 150 m depth at a distance of 60 km from the coast (Figure 10w). In a two-dimensional (distance to coast versus depth) view, the tilted orientation of the tracer structures at their early stage might suggest that vertical advection could be responsible for their formation (Figures 10w and 10z). However, our three-dimensional observations (Figures 9g and 12) imply that vertical advection is unlikely as a mechanism for the occurrence of the salinity structures. First of all, the structures cross isopycnals (Figure 10w). This should not be the case as advection moves water parcels predominantly along isopycnals. Second, the water properties (potential density, salinity, and temperature) in the structures do neither match those at the surface nor those at

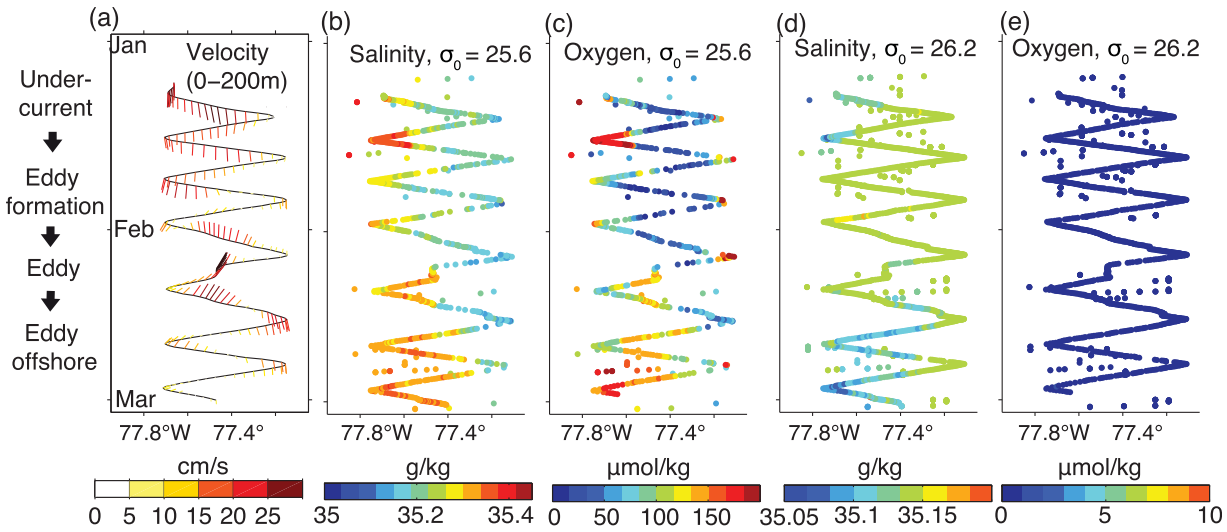

Figure 13. Hovmoeller diagram of the (a) depth-averaged (0–200 m) horizontal velocity in m/s, absolute salinity in g/kg at σ_0 range of (b) 25.61–25.63 kg/m^3 and (c) 26.19–26.2 kg/m^3, and (d) oxygen concentration in μmol/kg, (e) along 12°30′S measured by glider C (doted lines) and the ship-based CTD (single dots), which were taken close to the glider transect.

greater depths. Third isopycnals outcropping at the surface did not show density values as high as those in the structures throughout the entire measurement period.

Instead our observations suggest that lateral stirring by the rotational currents around the eddy periphery is a plausible mechanism for the formation of these structures. Figure 12 shows the formation of the salinity structures at the eddy edge (see black dashed box in Figure 9g) in more detail. At the early stage of the newly formed eddy, no salinity structures are found at the eddy edge (Figure 12a). However, 60 h later, a low-salinity structure shows up at the two southern transects (Figure 12b). Several days later, this feature is found along all transects (Figures 12c and 12d). The three-dimensional observational approach thus clearly indicates that the small-scale salinity structures at the eddy edge are formed by lateral advective flow around the eddy periphery. The potential density range and the temperature and salinity characteristics of the waters fit well to those of the low-salinity water seen in the first three transects of glider C described above (Figures 10b, 10e, and 10h). This further supports that lateral processes are at work.

The fact that low oxygen values and thus also no pronounced oxygen gradients are detectable below 80 m can explain why no small-scale oxygen structures are found below 80 m. However, at shallower depths, along-isopycnal oxygen gradients are indeed present (Figure 3c). Consequently, eddy-driven oxygen ventilation of the shallow near-coastal OMZ can be expected.

3.4.3. Eddy-Driven Ventilation of the Near-Coastal Oxygen Minimum Zone

In order to visualize the effects of the mesoscale stirring on the distributions of salinity and oxygen in more detail, we now analyze the temporal evolution of salinity and oxygen on two different isopycnals along the main transect (glider C) near 12°30′S (Figures 13b–13e). Both density surfaces are also shown in Figure 11 as white contours. The lighter density interface (25.6 kg/m^3) resides in relatively saline and oxygen-enriched water, while the denser density interface (26.2 kg/m^3) represents the oxygen depleted and relatively freshwaters within the OMZ. A close relationship between salinity and oxygen can be seen on the 25.6 kg/m^3 isopycnal, where high salinities go along with elevated oxygen concentrations. However, very close to the coast high oxygen concentrations are found which do not coincide with high salinities. This is due to the outcropping of the isopycnal into the well-oxygenated mixed layer close to the coast.

The temporal change of the depth-averaged (0–200 m) horizontal velocity along the glider track, which goes along with the eddy formation, can be seen in Figure 13a. By mid-February the velocities reveal an onshore component, which results in the onshore advection of high-salinity, well-oxygenated waters on the 25.6 kg/m^3 isopycnal. On this density surface, relatively low oxygen concentrations between 10 and 20 μmol/kg were observed in the center of the transect during January, while it showed values well-oxygenated ($>$100 μmol/kg) after the eddy had formed (Figures 13b and 13c). This can also be seen in the transects of the other gliders, which all show elevated oxygen values after the eddy had moved offshore (Figure 8n).

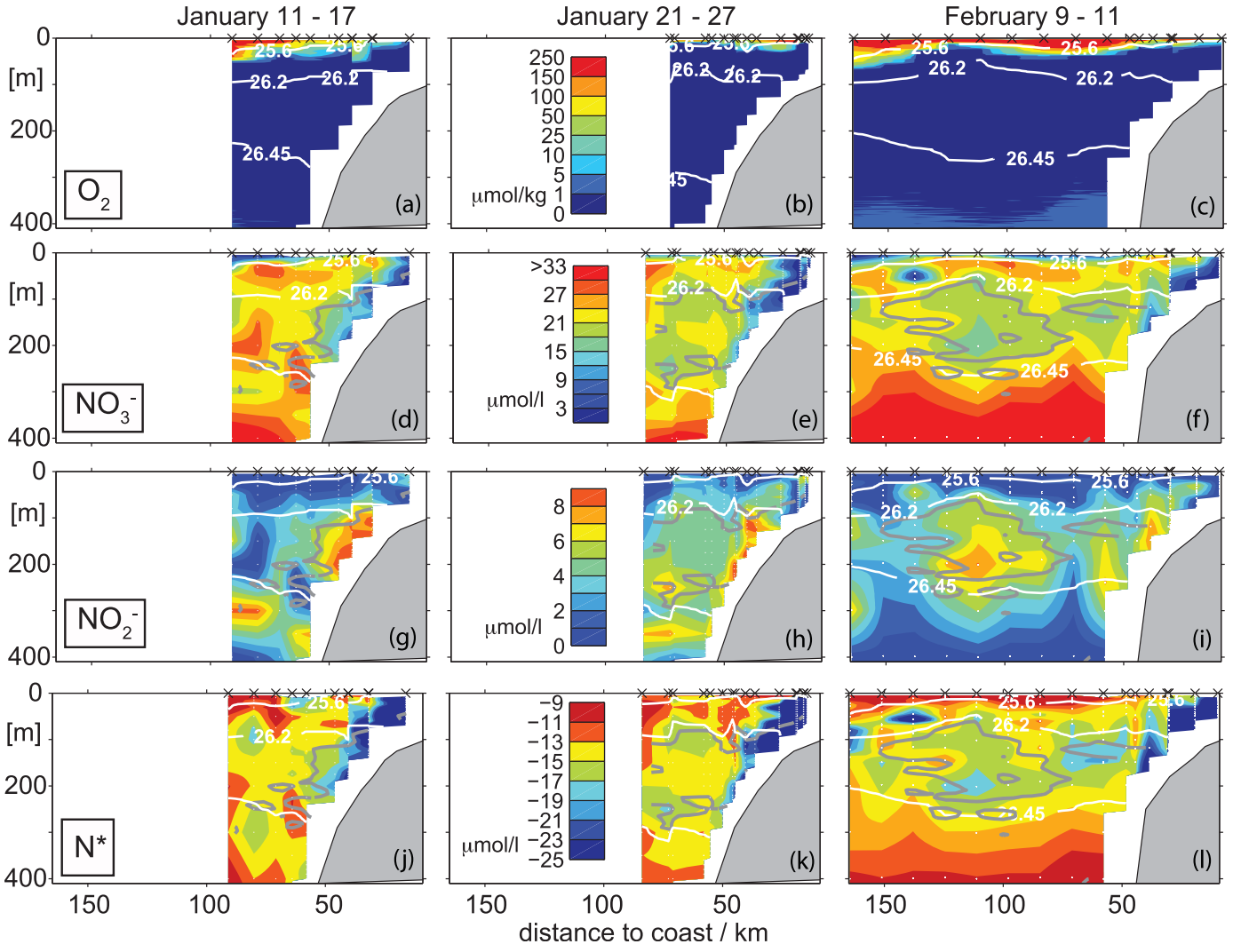

Figure 14. (first row) Oxygen in μmol/kg, (second row) nitrate (NO_3^-) in μmol/L, (third row) nitrite (NO_2^-) in μmol/L, (fourth row) nitrogen deficit ($N^* = (NO_3^- + NO_2^-) - 16PO_4^{3-}$) in μmol/L at three different time periods: (left column) prior to the eddy formation (11–17 January), (middle column) during the eddy formation (21–27 January), and when the eddy is fully developed (9–11 February). The positions of the nutrient measurements are marked with green dots in Figures 4a, 4g, and 4m. The white dots indicate position of the nutrient measurements. The grey line shows the $fPV = 1.1 \times 10^{-14}$ $1/s^4$ contour.

At greater depths, on the 26.2 kg/m^3 isopycnal, changes in salinity are also observed during the measurement period. After the eddy is formed, a fresher water mass shows up (see discussion in section 3.4.2). However, more importantly no significant correlation between oxygen and salinity on the 26.2 kg/m^3 isopycnal can be established, as the oxygen concentrations (<1 μmol/kg) are below the detection limit. Consequently, no pronounced oxygen structures are advected on this density surface.

In summary, the eddy clearly supplied oxygen-enriched waters to the near-coastal OMZ on the 25.6 kg/m^3 isopycnal, which points to the importance of mesoscale stirring for the ventilation of the near-coastal OMZ off Peru.

3.5. Impact of the Horizontal Circulation on the Distributions of Nitrate, Nitrite, and Nitrogen Deficit

The changing circulation during the eddy formation also impacts the nitrate (NO_3^-), nitrite (NO_3^-), and nitrogen deficit (N*) distributions (Figure 14). N* is often used as an indicator for nitrogen sink/source processes in the water column [*Gruber and Sarmiento*, 1997]. However, it is important to note that enhanced N* values are not an indicator of active nitrogen loss processes but represent the accumulated nitrogen loss of the past. Here we define $N^* = (NO_3^- + NO_2^-) - 16PO_4^{3-}$, with ($PO_4^{3-}$) being phosphate, following *Altabet et al.* [2012] and *Stramma et al.* [2013] in order to allow a direct comparison to their findings. We focus on the

exchange of NO_3^-, NO_2^-, and N* between the continental slope and the open ocean, but not on the upper shelf (<150 m), where the eddy has less influence on the water mass distribution (sections 3.2 and 3.4).

Prior to the eddy formation NO_3^- (NO_2^-) concentrations were mainly above 21 μmol/L (below 4 μmol/L) offshore of the continental slope (Figures 14d and 14g). In contrast, NO_3^- (NO_2^-) concentrations below 18 μmol/L (above 7 μmol/L) are observed at the continental slope, especially near the bottom, coinciding with N* values below -17 μmol/L (Figure 14j). Given that all three parameters show along-isopycnal gradients, eddy-driven crossshore fluxes can be expected. Note that the NO_3^- and N* concentrations decrease toward the coast along-isopycnals, while NO_2^- concentrations increase. Thus, onshore fluxes of NO_3^- and N* (which corresponds to offshore fluxes of nitrogen deficit waters) and offshore fluxes of NO_2^- are expected.

The eddy formation is associated with acrossshore velocities. They cause an exchange of waters across the continental slope, leading to a change in the nutrient distribution (Figure 14, middle column). As a result, NO_3^- (NO_2^-) concentrations as low as 15 μmol/L (between 4 and 8 μmol/L) are found offshore between 50 and 300 m depth (Figures 14e and 14h). Note that the low *PV* distribution (indicated by the grey contour in Figure 14) supports our interpretation that these waters originate from bottom boundary layer along the continental slope (see section 3.3).

After the eddy has formed, a transect through the eddy was obtained (Figure 14, right column). We observe NO_3^- concentrations between 15 and 21 μmol/L (Figure 14f), NO_2^- concentrations of up to 8 μmol/L (Figure 14i), and a nitrogen deficit near 17 μmol/L close to the core of the newly formed eddy (Figure 14l).

In summary, similar to the low *PV* originating from the bottom boundary at the continental slope, the eddy also advects nitrogen deficient waters from the region into the open ocean.

4. Discussion

To date, only indirect observational evidence for the importance of the PCUC for the generation of subsurface anticyclonic eddies off Peru has been obtained, based both on water mass analyses [*Johnson and McTaggart*, 2010] and the fact that most anticyclones are first detected close to the shelf [*Chaigneau et al*., 2011]. The aim of this study is to provide direct observational evidence that subsurface anticyclones off Peru are indeed formed by instability of the PCUC. The study is based on a multiplatform four-dimensional observational approach. The extensive data set described here allows a detailed description of the eddy formation process and its impact on the near-coastal salinity, oxygen, and nutrient distributions.

The observations suggest that flow separation due to a sharp bend of the continental slope plays an important role for the eddy generation. This implies that the strength of the PCUC is an important parameter, which determines whether a subsurface anticyclone may be generated at this location by flow separation or not. Indeed we observed a relatively strong PCUC (~0.25 m/s observed core speed, long-term mean ~0.15 m/s [*Chaigneau et al*., 2013]) prior to the eddy formation. Remotely forced coastal trapped waves strongly influence the PCUC [*Chaigneau et al*., 2013; *Pietri et al*., 2014] and thus might play an important role in modulating the strength of the subsurface anticyclonic eddy formation process.

A numerical modeling study by *Colas et al*. [2012] indicates that subsurface anticyclonic eddies contribute to the eddy variability off Peru. The authors found anticyclonic vorticity to dominate off Peru with a maximum between 100 and 150 m depth. They relate this finding to subsurface anticyclonic coherent vortices formed by instability of the PCUC. This supports the view that these coherent eddies are important in this region. Clearly, our study is limited to a single eddy formation event. The representativeness of this event for the generation of subsurface anticyclonic eddies in the Peruvian upwelling system thus remains an open question. However, in a recent study, *Hormazabal et al*. [2013] investigate the properties and origin of subsurface anticyclonic eddies off central Chile using hydrographic observations, satellite altimetry, and a regional eddy-resolving ocean model. In their study, observations of two subsurface anticyclonic eddies are presented. Both eddies were first detected close to a sharp coastline variation near 37°S, thus we suggest that flow separation might be responsible for their formation. In general, high mesoscale variability is found off Peru [*Penven et al*., 2005]. We expect that beside flow separation also other instability and forcing mechanisms contribute to the overall eddy field as pointed out by *Liang et al*. [2012] for the northeastern tropical Pacific.

The result that flow separation might be responsible for the formation of subsurface coherent anticyclones in boundary currents is in line with a study by *D'Asaro* [1988] and a recent very high-resolution modeling experiment of the California Undercurrent by *Molemaker et al*. [2015]. Both studies investigate the generation mechanism of submesoscale coherent vortices and the boundary currents separate behind sharp topographic bends. *Molemaker et al*. [2015] point out the complexity of the full eddy generation mechanism, which involves not only boundary current separation but also submesoscale instabilities and upscale flow self-organization. Several aspects of their results agree with the observations presented here: We find unorganized small-scale velocity structures prior to the eddy formation; a much more organized coherent structure at a later stage; and a growth of the first coherent eddy structure to a much larger eddy within a few days (Figures 4j and 4m). An interesting finding by *Molemaker et al*. [2015] is the importance of the frictional boundary layer for the generation of anticyclonic vorticity and low *PV* found in the eddy core. This was already suggested by *D'Asaro* [1988]. It implies that a large amount of the core water might originate from the bottom boundary layer at the continental slope. In agreement, we observe very low *PV* in water residing on the topography of the continental slope prior to the eddy formation. Evidence is presented showing that this water ends up in the eddy core during its formation. Thus, our observations support the findings of *D'Asaro* [1988] and *Molemaker et al*. [2015] regarding the bottom boundary layer being an important source region of the eddy core water.

The nutrient measurements taken during the formation of the anticyclonic subsurface eddy should give new insights into the role of these eddies for the nitrogen cycling and loss off Peru. In general, the water masses on the continental margin off Peru and Chile are increasingly depleted in biologically available nitrogen during their poleward transport within the PCUC due to nitrogen-cycling processes [*Zamora et al*., 2012; *Kalvelage et al*., 2013; *Loescher et al*., 2014], and near-coastal nutrients measurements off Peru often show reduced NO_3^- and N* concentrations in the bottom boundary layer [*Codispoti and Christensen*, 1985; *Hamersley et al*., 2007; *Lam et al*., 2009; *Franz et al*., 2012; *Loescher et al*., 2014]. This is also the case for the nutrient values present in this study (Figure 14), where enhanced nitrogen deficits are observed close to the topography of the continental slope.

In a relatively young eddy close to the shelf near 16°S, *Stramma et al*. [2013] observe a nitrogen deficit anomalies of 35 μmol/L at 50 m and 20 μmol/L in 150 m depth, as well as NO_3^- and NO_2^- core concentrations of <5 and ~10 μmol/L, respectively. They suggest that the high N* and low NO_3^- is due to enhanced nitrogen loss activity in the eddy. Our observations could be interpreted such that a substantial part of the nitrogen deficits documented further offshore both close to a mesoscale eddy [*Altabet et al*., 2012] and inside anticyclonic subsurface eddies [*Stramma et al*., 2013] might result from nitrogen loss processes on the upper continental slope and shelf region [*Kalvelage et al*., 2013], and are subsequently transported toward the open ocean by the eddy.

While measured nitrogen loss rates reported in shelf waters are high (0.05–0.5 μmol/L/d) [*Hamersley et al*., 2007; *Kalvelage et al*., 2013] and in combination with benthic nitrogen loss [*Bohlen et al*., 2011] can significantly change N* within days to weeks, the nitrogen loss reported from open ocean is usually well below 0.01 μmol/L/d [*Ward et al*., 2009; *Canfield et al*., 2010; *Kalvelage et al*., 2013].

In order to distinguish between anomalies that originate at the coast or are induced in the eddy itself, observations of the initial core water mass properties are crucial, but have been missing so far in previous studies. Thus, in future studies, one should strive to observe the full eddy life cycle including the formation and offshore propagation. In particular, the source waters of the eddy core, which are known to change within the PCUC along the coastline [*Zamora et al*., 2012], should be captured. In a recent study by *Bourbonnais et al*. [2015], the authors sampled one eddy during two occasions 1 month apart from each other. They find a reduction of NO_3- of about 4 μmol/L in the density range between 26.2 and 26.3 kg/m^3 between the two surveys. However, it remains unexplained how much of the already enhanced nitrogen deficit of 35 μmol/L during the first survey results from coastal and/or eddy-induced nitrogen loss processes.

In this study, we describe in detail that eddy-driven along-isopycnal stirring due to both rotational currents around the eddy periphery and water mass trapping inside the eddy results in an exchange of water masses between the continental slope and the open ocean. The export of nitrogen deficient water from the continental margin to the open ocean provides a mechanism which might help to explain the observed discrepancies between nitrogen loss activity and accumulated nitrogen deficit [*Kalvelage et al*., 2013]. Thus,

mesoscale eddies might be crucial in resupplying NO_3^- to the productive continental margin at depth where nitrogen loss processes and organic matter export are thought to be highest [*Kalvelage et al*., 2013].

Our observations show that the horizontal circulation has a large effect on the near-coastal salinity and oxygen distributions and results in the formation of various small-scale salinity and oxygen structures. *Pietri et al*. [2013] discuss the formation of small-scale salinity structures in the Peruvian upwelling regime at around 14°S similar to the ones we describe in this study. Our observations confirm their interpretation that lateral stirring of along-isopycnal salinity gradients by mesoscale eddies is mainly responsible for the formation of the fine-scale structures. Their additional hypothesis that vertical advective motion driven by submesoscale frontal subduction processes might be responsible for the formation of the salinity structures cannot be confirmed by our study. This hypothesis, however, is discussed in recent literature [*Mechoso et al*., 2014; *Messié and Chavez*, 2014]. Here we want to note that the interpretation of two-dimensional small-scale tracer structures by a single glider has to be done with utmost caution, as horizontal processes such as mesoscale stirring can form a wide range of tracer structures. However, our three-dimensional approach might help to interpret small-scale salinity and oxygen structures found in future high-resolution two-dimensional observations.

Quantitative eddy-driven oxygen fluxes cannot be estimated from our observations due to the short time period, which only covers one single eddy event. However, the signature of the eddy-driven oxygen ventilation of the near-coastal OMZ is clearly visible in our data set. *Stramma et al*. [2010] and *Brandt et al*. [2015] came up with rough oxygen budget estimates based on climatological oxygen distributions and an assumed value for the eddy diffusivity. They suggest that 45% of total oxygen supply in the eastern tropical South Pacific OMZ is provided by eddy-driven lateral mixing.

5. Summary and Conclusions

The formation of a subsurface anticyclonic eddy in the Peru-Chile Undercurrent in January and February 2013 is investigated based on four-dimensional multiple platform observations. The main results are listed below:

1. A strong Peru-Chile Undercurrent with maximum poleward velocities of about 0.25 m/s was observed in early January 2013 off Peru. Isolated oxygen patches are found within the oxygen minimum zones. The differential advection along isopycnals in the vertically sheared upper part of the Peru-Chile Undercurrent is suggested to be their formation mechanism.
2. After 20 January, a subsurface anticyclonic eddy was shed by the Peru-Chile Undercurrent. The eddy core was characterized by potential vorticity close to zero, which seems to have originated from the bottom boundary layer on the continental slope. The eddy formed just downstream of a sharp topographic bend of the 400 m isobath. This suggests flow separation as likely eddy formation mechanism.
3. The eddy-induced circulation strongly modifies the near-coastal salinity and oxygen distributions. Horizontal rotational currents around the eddy periphery (mesoscale stirring) result in the formation of small-scale salinity structures at the eddy edge. Across-shelf velocities advect the saline and well-oxygenated Subtropical Surface Water within the thermocline toward the coast. This points to the importance of mesoscale eddies for the ventilation of the upper near-coastal oxygen minimum zone off Peru.
4. The eddy core shows temperature and salinity values characteristic of Equatorial Subsurface Water and oxygen concentrations <1 μmol/kg. Additionally, an elevated nitrogen deficit of about 17 μmol/L and enhanced NO_2^- concentrations near 7 μmol/L are found within the eddy just after its formation. They are thought to result from near-shelf nitrogen loss processes prior the eddy formation.

Our study highlights the impact of the subsurface anticyclonic eddy shed by the Peru-Chile Undercurrent on the tracer distributions in the Peruvian oxygen minimum zone both on a local scale and on larger scales. On one hand, the eddy stirs local tracer (salinity, oxygen, and nutrient) gradients. On the other hand, it traps water mass properties (e.g., vanishing oxygen, enhanced NO_2- concentrations, and nitrogen deficits) from the upper continental slope and transports them offshore into the open ocean oxygen minimum zone during its westward propagation. As anticyclonic subsurface eddies may exist for several months and travel large distances [*Stramma et al*., 2014], they can carry water mass properties to very remote places. A large number of studies highlight the general importance of eddies for modulating both biogeochemical productivity and biogeochemical cycles [*Jenkins*, 1988; *Falkowski et al*., 1991; *Oschlies and Garcon*, 1998;

McGillicuddy et al., 1998, 2007; *Lathuilière et al*., 2010; *Gruber et al*., 2011; *Gaube et al*., 2014]. However, most global biogeochemical model studies investigating oxygen minimum zones use models which do not resolve mesoscale eddies. Thus, their effects have to be parameterized. This might cause uncertainties in forecasting long-term oxygen trends [*Stramma et al*., 2008, 2010] or in the response of oxygen minimum zones to a changing climate [*Stramma et al*., 2012]. More recent high-resolution model studies exist which have sufficiently high resolution to allow eddies to evolve [*Dietze and Loeptien*, 2013; *Montes et al*., 2014; *Duteil et al*., 2014]. However, these studies focus mostly on the improvements in representing the equatorial current band as a result of enhanced resolution as these currents seem to have a large impact in reducing the bias between simulated and observed nutrient and oxygen distributions. We suggest using these high-resolution simulations to focus on the large-scale effect of mesoscale eddies on oxygen minimum zone dynamics. This is difficult to assess quantitatively even with high-resolution observations. Our high-resolution four-dimensional observational study can help to validate and improve these simulations, since we provide observations of the variability seen in physical and biogeochemical parameters. This study highlights the need for high spatiotemporal resolution observations in eastern boundary upwelling regimes in order to understand the mechanisms driving the observed fast changes in physical and biogeochemical parameters.

Acknowledgments

This work is a contribution of the Sonderforschungsbereich 754 "Climate-Biogeochemistry Interactions in the Tropical Ocean" (www.sfb754.de), which is funded by the Deutsche Forschungsgemeinschaft (DFG). We are grateful to the Peruvian authorities for the permission to carry out scientific work in their national waters. Special thanks go to the captain and the crew of the R/V Meteor for their support during the M92 and M93 cruises. We are grateful to Niels Peter Revsbech for providing the STOX sensors. We further thank Tim Kalvelage and Gabriele Klockgether for technical assistance, Johannes Hahn for his support with the glider optode calibration, and Matthias Krueger for the processing the vessel mounted ADCP data. We thank Anthony Bosse, Liam Brannigan, Julius Busecke, Yonss Jose, and two anonymous reviewers for helpful suggestions to improve the manuscript. The used data sets are stored on the Kiel Ocean Science Information System (OSIS, https://portal.geomar.de/kdmi, datamanagement@geomar.de) and can be accessed upon request. According to the SFB 754 data policy (https://www.sfb754.de/de/data), all data associated with this publication will be published at a world data center (www.pangaea.de, search project:sfb754) when the paper is accepted and published.

References

Altabet, M. A., E. Ryabenko, L. Stramma, D. W. R. Wallace, M. Frank, P. Grasse, and G. Lavik (2012), An eddy-stimulated hotspot for fixed nitrogen-loss from the Peru oxygen minimum zone, *Biogeosciences*, *9*(12), 4897–4908, doi:10.5194/bg-9-4897-2012.

Bittig, H. C., B. Fiedler, R. Scholz, G. Krahmann, and A. Körtzinger (2014), Time response of oxygen optodes on profiling platforms and its dependence on flow speed and temperature, *Limnol. Oceanogr. Methods*, *12*(8), 617–636, doi:10.4319/lom.2014.12.617.

Bohlen, L., A. Dale, S. Sommer, T. Mosch, C. Hensen, A. Noffke, F. Scholz, and K. Wallmann (2011), Benthic nitrogen cycling traversing the Peruvian oxygen minimum zone, *Geochim. Cosmochim. Acta*, *75*(20), 6094–6111, doi:10.1016/j.gca.2011.08.010.

Bosse, A., P. Testor, L. Mortier, L. Prieur, V. Taillandier, F. d'Ortenzio, and L. Coppola (2015), Spreading of Levantine intermediate waters by submesoscale coherent vortices in the northwestern Mediterranean Sea as observed with gliders, *J. Geophys. Res. Oceans*, *120*, 1599–1622, doi:10.1002/2014JC010263.

Bourbonnais, A., M. A. Altabet, C. N. Charoenpong, J. Larkum, H. Hu, H. W. Bange, and L. Stramma (2015), N-loss isotope effects in the Peru oxygen minimum zone studied using a mesoscale eddy as a natural tracer experiment, *Global Biogeochem. Cycles*, *29*, 793–811, doi:10.1002/2014GB005001.

Bower, A. S., L. Armi, and I. Ambar (1995), Direct evidence of meddy formation off the southwestern coast of Portugal, *Deep Sea Res., Part I*, *42*(9), 1621–1630, doi:10.1016/0967-0637(95)00045-8.

Bower, A. S., L. Armi, and I. Ambar (1997), Lagrangian observations of meddy formation during a mediterranean undercurrent seeding experiment, *J. Phys. Oceanogr.*, *27*(12), 2545–2575, doi:10.1175/1520-0485(1997)027<2545:LOOMFD>2.0.CO;2.

Brandt, P., et al. (2015), On the role of circulation and mixing in the ventilation of oxygen minimum zones with a focus on the eastern tropical north Atlantic, *Biogeosciences*, *12*(2), 489–512, doi:10.5194/bg-12-489-2015.

Brink, K., D. Halpern, A. Huyer, and R. L. Smith (1983), The physical environment of the Peruvian upwelling system, *Prog. Oceanogr.*, *12*, 285–305.

Canfield, D. E., F. J. Stewart, B. Thamdrup, L. De Brabandere, T. Dalsgaard, E. F. Delong, N. P. Revsbech, and O. Ulloa (2010), A cryptic sulfur cycle in oxygen-minimum–zone waters off the Chilean coast, *Science*, *330*(6009), 1375–1378, doi:10.1126/science.1196889.

Chaigneau, A., A. Gizolme, and C. Grados (2008), Mesoscale eddies off Peru in altimeter records: Identification algorithms and eddy spatio-temporal patterns, *Prog. Oceanogr.*, *79*(2–4), 106–119, doi:10.1016/j.pocean.2008.10.013.

Chaigneau, A., M. Le Texier, G. Eldin, C. Grados, and O. Pizarro (2011), Vertical structure of mesoscale eddies in the eastern South Pacific Ocean: A composite analysis from altimetry and argo profiling floats, *J. Geophys. Res.*, *116*, C11025, doi:10.1029/2011JC007134.

Chaigneau, A., N. Dominguez, G. Eldin, L. Vasquez, R. Flores, C. Grados, and V. Echevin (2013), Near-coastal circulation in the Northern Humboldt Current System from shipboard ADCP data, *J. Geophys. Res. Oceans*, *118*, 5251–5266, doi:10.1002/jgrc.20328.

Chavez, F. P., A. Bertrand, R. Guevara-Carrasco, P. Soler, and J. Csirke (2008), The northern Humboldt Current System: Brief history, present status and a view towards the future, *Prog. Oceanogr.*, *79*(2–4), 95–105, doi:10.1016/j.pocean.2008.10.012.

Cline, J., and F. Richards (1972), Oxygen deficient conditions and nitrate reduction in the eastern tropical North Pacific Ocean, *Limnol. Oceanogr.*, *17*, 885–900.

Codispoti, L., and J. Christensen (1985), Nitrification, denitrification and nitrous oxide cycling in the eastern tropical South Pacific Ocean, *Mar. Chem.*, *16*, 509–525.

Codispoti, L., and T. Packard (1980), Denitrification rates in the eastern tropical south-pacific, *J. Mar. Res.*, *38*, 453–477.

Colas, F., J. McWilliams, X. Capet, and J. Kurian (2012), Heat balance and eddies in the Peru-Chile current system, *Clim. Dyn.*, *39*(1–2), 509–529, doi:10.1007/s00382-011-1170-6.

Combes, V., S. Hormazabal, and E. Di Lorenzo (2015), Interannual variability of the subsurface eddy field in the southeast pacific, *J. Geophys. Res. Oceans*, *120*, 4907–4924, doi:10.1002/2014JC010265.

D'Asaro, E. A. (1988), Generation of submesoscale vortices: A new mechanism, *J. Geophys. Res.*, *93*(C6), 6685–6693, doi:10.1029/JC093iC06p06685.

Dietze, H., and U. Loeptien (2013), Revisiting "nutrient trapping" in global coupled biogeochemical ocean circulation models, *Global Biogeochem. Cycles*, *27*, 265–284, doi:10.1002/gbc.20029.

Ducet, N., P. Y. Le Traon, and G. Reverdin (2000), Global high-resolution mapping of ocean circulation from Topex/Poseidon and ERS-1 and −2, *J. Geophys. Res.*, *105*(C8), 19,477–19,498, doi:10.1029/2000JC900063.

Duteil, O., F. U. Schwarzkopf, C. W. Böning, and A. Oschlies (2014), Major role of the equatorial current system in setting oxygen levels in the eastern tropical Atlantic Ocean: A high-resolution model study, *Geophys. Res. Lett.*, *41*, 2033–2040, doi:10.1002/2013GL058888.

Falkowski, P. G., D. Ziemann, Z. Kolber, and P. K. Bienfang (1991), Role of eddy pumping in enhancing primary production in the ocean, *Nature*, *352*(6330), 55–58.
Fiedler, P. C., and L. D. Talley (2006), Hydrography of the eastern tropical pacific: A review, *Prog. Oceanogr.*, *69*(2–4), 143–180, doi:10.1016/j.pocean.2006.03.008.
Fonseca, T. R. (1989), An overview of the poleward undercurrent and upwelling along the Chilean Coast, in *Poleward Flows Along Eastern Ocean Boundaries, Coastal Estuarine Stud*., vol. 34, edited by S. J. Neshyba et al., pp. 203–228, Springer, N. Y.
Franz, J., G. Krahmann, G. Lavik, P. Grasse, T. Dittmar, and U. Riebesell (2012), Dynamics and stoichiometry of nutrients and phytoplankton in waters influenced by the oxygen minimum zone in the eastern tropical pacific, *Deep Sea Res., Part I*, *62*, 20–31, doi:10.1016/j.dsr.2011.12.004.
Fuenzalida, R., W. Schneider, J. Garcés-Vargas, L. Bravo, and C. Lange (2009), Vertical and horizontal extension of the oxygen minimum zone in the eastern south pacific ocean, *Deep Sea Res., Part II*, *56*(16), 992–1003, doi:10.1016/j.dsr2.2008.11.001.
Garau, B., S. Ruiz, W. G. Zhang, A. Pascual, E. Heslop, J. Kerfoot, and J. Tintoré (2011), Thermal lag correction on slocum CTD glider data, *J. Atmos. Oceanic Technol.*, *28*(9), 1065–1071, doi:10.1175/JTECH-D-10-05030.1.
Gaube, P., D. J. McGillicuddy, D. B. Chelton, M. J. Behrenfeld, and P. G. Strutton (2014), Regional variations in the influence of mesoscale eddies on near-surface chlorophyll, *J. Geophys. Res. Oceans*, *119*, 8195–8220, doi:10.1002/2014JC010111.
Gill, A. (1982), *Atmosphere-Ocean Dynamics, Int. Geophys. Ser.*, *30*, Elsevier Sci., N. Y.
Grasshoff, K., M. Ehrhardt, and K. Kremling (1983), *Methods of Seawater Analysis*, 419 pp., Verlag Chem., Weinheim, Germany.
Gruber, N. (2008), The marine nitrogen cycle: Overview and challenges, in *Nitrogen in the Marine Environment*, 2nd ed., edited by D. G. Capone et al., chap. 1, pp. 1–50, Academic, San Diego, Calif.
Gruber, N., and J. L. Sarmiento (1997), Global patterns of marine nitrogen fixation and denitrification, *Global Biogeochem. Cycles*, *11*(2), 235–266, doi:10.1029/97GB00077.
Gruber, N., Z. Lachkar, H. Frenzel, P. Marchesiello, M. Munnich, J. C. McWilliams, T. Nagai, and G.-K. Plattner (2011), Eddy-induced reduction of biological production in eastern boundary upwelling systems, *Nat. Geosci.*, *4*(11), 787–792.
Gunther, E. R. (1936), A report on oceanographic investigations in the Peru coastal current, *Discovery Rep.*, *13*, 107–276.
Gutiérrez, D., E. Enríquez, S. Purca, L. Quipúzcoa, R. Marquina, G. Flores, and M. Graco (2008), Oxygenation episodes on the continental shelf of central Peru: Remote forcing and benthic ecosystem response, *Prog. Oceanogr.*, *79*(2–4), 177–189, doi:10.1016/j.pocean.2008.10.025.
Hahn, J., P. Brandt, R. J. Greatbatch, G. Krahmann, and A. Körtzinger (2014), Oxygen variance and meridional oxygen supply in the Tropical North East Atlantic oxygen minimum zone, *Clim. Dyn.*, *43*, 2999–3024.
Hamersley, M. R., G. Lavik, D. Woebken, J. E. Rattray, E. C. Hopmans, and J. S. Sinninghe (2007), Anaerobic ammonium oxidation in the Peruvian oxygen minimum zone, *Limnol. Oceanogr.*, *52*(3), 923–933, doi:10.4319/lo.2007.52.3.0923.
Holte, J., F. Straneo, C. Moffat, R. Weller, and J. T. Farrar (2013), Structure and surface properties of eddies in the southeast Pacific Ocean, *J. Geophys. Res. Oceans*, *118*, 2295–2309, doi:10.1002/jgrc.20175.
Hormazabal, S., V. Combes, C. E. Morales, M. A. Correa-Ramirez, E. Di Lorenzo, and S. Nuñez (2013), Intrathermocline eddies in the coastal transition zone off central Chile (31–41°S), *J. Geophys. Res. Oceans*, *118*, 4811–4821, doi:10.1002/jgrc.20337.
Hoskins, B. J. (1974), The role of potential vorticity in symmetric stability and instability, *Q. J. R. Meteorol. Soc.*, *100*(425), 480–482, doi:10.1002/qj.49710042520.
Huyer, A., M. Knoll, T. Paluzkiewicz, and R. L. Smith (1991), The Peru undercurrent: A study in variability, *Deep Sea Res., Part A*, *39*, 247–279.
Jenkins, W. J. (1988), Nitrate flux into the euphotic zone near Bermuda, *Nature*, *331*(6156), 521–523.
Johnson, G. C., and K. E. McTaggart (2010), Equatorial pacific 13°C water eddies in the eastern subtropical South Pacific Ocean, *J. Phys. Oceanogr.*, *40*(1), 226–236, doi:10.1175/2009JPO4287.1.
Johnson, G. C., J. M. Toole, and N. G. Larson (2007), Sensor corrections for sea-bird SBE-41CP and SBE-41 CTDs, *J. Atmos. Oceanic Technol.*, *24*(6), 1117–1130, doi:10.1175/JTECH2016.1.
Kalvelage, T., G. Lavik, P. Lam, S. Contreras, L. Arteaga, C. R. Loscher, A. Oschlies, A. Paulmier, L. Stramma, and M. M. M. Kuypers (2013), Nitrogen cycling driven by organic matter export in the south pacific oxygen minimum zone, *Nat. Geosci.*, *6*(3), 228–234.
Karstensen, J. (2004), Formation of the South Pacific shallow salinity minimum: A southern ocean pathway to the tropical Pacific, *J. Phys. Oceanogr.*, *34*, 2398–2412, doi:10.1175/JPO2634.1.
Karstensen, J., and D. Quadfasel (2002), Formation of southern hemisphere thermocline waters: Water mass conversion and subduction, *J. Phys. Oceanogr.*, *32*(11), 3020–3038, doi:10.1175/1520-0485(2002)032 < 3020:FOSHTW>2.0.CO;2.
Karstensen, J., L. Stramma, and M. Visbeck (2008), Oxygen minimum zones in the eastern tropical Atlantic and Pacific oceans, *Prog. Oceanogr.*, *77*(4), 331–350, doi:10.1016/j.pocean.2007.05.009.
Karstensen, J., B. Fiedler, F. Schütte, P. Brandt, A. Körtzinger, G. Fischer, R. Zantopp, J. Hahn, M. Visbeck, and D. Wallace (2015), Open ocean dead zones in the tropical North Atlantic Ocean, *Biogeosciences*, *12*(8), 2597–2605, doi:10.5194/bg-12-2597-2015.
Kessler, W. S. (2006), The circulation of the eastern tropical Pacific: A review, *Prog. Oceanogr.*, *69*(2–4), 181–217, doi:10.1016/j.pocean.2006.03.009.
Kinsella, E. D., A. E. Hay, and W. W. Denner (1987), Wind and topographic effects on the Labrador current at Carson canyon, *J. Geophys. Res.*, *92*(C10), 10,853–10,869, doi:10.1029/JC092iC10p10853.
Klein, P., and G. Lapeyre (2009), The oceanic vertical pump induced by mesoscale and submesoscale turbulence, *Annu. Rev. Mar. Sci.*, *1*(1), 351–375, doi:10.1146/annurev.marine.010908.163704.
Lam, P., G. Lavik, M. M. Jensen, J. van de Vossenberg, M. Schmid, D. Woebken, D. Gutiérrez, R. Amann, M. S. M. Jetten, and M. M. M. Kuypers (2009), Revising the nitrogen cycle in the Peruvian oxygen minimum zone, *Proc. Natl. Acad. Sci. U. S. A.*, *106*(12), 4752–4757, doi:10.1073/pnas.0812444106.
Lathuilière, C., V. Echevin, M. Lévy, and G. Madec (2010), On the role of the mesoscale circulation on an idealized coastal upwelling ecosystem, *J. Geophys. Res.*, *115*, C09018, doi:10.1029/2009JC005827.
Liang, J.-H., J. C. McWilliams, J. Kurian, F. Colas, P. Wang, and Y. Uchiyama (2012), Mesoscale variability in the northeastern tropical Pacific: Forcing mechanisms and eddy properties, *J. Geophys. Res.*, *117*, C07003, doi:10.1029/2012JC008008.
Loescher, C. R., et al. (2014), Facets of diazotrophy in the oxygen minimum zone waters off Peru, *ISME J.*, *8*(11), 2180–2192.
Luyten, J. R., J. Pedlosky, and H. Stommel (1983a), The ventilated thermocline, *J. Phys. Oceanogr.*, *13*(2), 292–309, doi:10.1175/1520-0485(1983)013 < 0292:TVT>2.0.CO;2.
Luyten, J. R., J. Pedlosky, and H. Stommel (1983b), Climatic inferences from the ventilated thermocline, *Clim. Change*, *5*(2), 183–191.
Marshall, D. P., and C. E. Tansley (2001), An implicit formula for boundary current separation, *J. Phys. Oceanogr.*, *31*(6), 1633–1638, doi:10.1175/1520-0485(2001)031 < 1633:AIFFBC>2.0.CO;2.
McDougall, T. J., and P. M. Barker (2011), Getting started with TEOS-10 and the Gibbs seawater (GSW) oceanographic toolbox, *Rep. SCOR/IAPSO WG127*, 28 pp., doi:10.1002/2014JC010066. [Available at www.TEOS-10.org.]

McDowell, S. E., and H. T. Rossby (1978), Mediterranean water: An intense mesoscale eddy off the Bahamas, *Science*, *202*(4372), 1085–1087, doi:10.1126/science.202.4372.1085.
McGillicuddy, D., A. Robinson, D. Siegel, H. Jannasch, R. Johnson, T. Dickey, J. McNeil, A. Michaels, and A. Knap (1998), Influence of mesoscale eddies on new production in the Sargasso Sea, *Nature*, *394*, 263–265.
McGillicuddy, D. J., et al. (2007), Eddy/wind interactions stimulate extraordinary mid-ocean plankton blooms, *Science*, *316*(5827), 1021–1026, doi:10.1126/science.1136256.
McWilliams, J. C. (1985), Submesoscale, coherent vortices in the ocean, *Rev. Geophys.*, *23*(2), 165–182, doi:10.1029/RG023i002p00165.
Mechoso, C. R., et al. (2014), Ocean–cloud–atmosphere–land interactions in the southeastern Pacific: The vocals program, *Bull. Am. Meteorol. Soc.*, *95*(3), 357–375, doi:10.1175/BAMS-D-11-00246.1.
Merckelbach, L., D. Smeed, and G. Griffiths (2010), Vertical water velocities from underwater gliders, *J. Atmos. Oceanic Technol.*, *27*(3), 547–563, doi:10.1175/2009JTECHO710.1.
Messié, M., and F. Chavez (2014), Seasonal regulation of primary production in eastern boundary upwelling systems, *Prog. Oceanogr.*, *134*, 1–18.
Molemaker, M. J., J. C. McWilliams, and W. K. Dewar (2015), Submesoscale instability and generation of mesoscale anticyclones near a separation of the California undercurrent, *J. Phys. Oceanogr.*, *45*, 613–629, doi:10.1175/JPO-D-13-0225.1.
Montes, I., F. Colas, X. Capet, and W. Schneider (2010), On the pathways of the equatorial subsurface currents in the eastern equatorial pacific and their contributions to the Peru-Chile undercurrent, *J. Geophys. Res.*, *115*, C09003, doi:10.1029/2009JC005710.
Montes, I., B. Dewitte, E. Gutknecht, A. Paulmier, I. Dadou, A. Oschlies, and V. Garçon (2014), High-resolution modeling of the eastern tropical Pacific oxygen minimum zone: Sensitivity to the tropical oceanic circulation, *J. Geophys. Res. Oceans*, *119*, 5515–5532, doi:10.1002/2014JC009858.
Okubo, A. (1970), Horizontal dispersion of floatable particles in the vicinity of velocity singularities such as convergences, *Deep Sea Res. Oceanogr. Abstr.*, *17*(3), 445–454, doi:10.1016/0011-7471(70)90059-8.
Oschlies, A., and V. Garcon (1998), Eddy-induced enhancement of primary production in a model of the north Atlantic Ocean, *Nature*, *394*, 266–269.
Paulmier, A., and D. Ruiz-Pino (2009), Oxygen minimum zones (OMZS) in the modern ocean, *Prog. Oceanogr.*, *80*(3–4), 113–128, doi:10.1016/j.pocean.2008.08.001.
Pedlosky, J. (1979), *Geophysical Fluid Dynamics*, 624 pp., Springer, N. Y.
Pennington, J. T., K. L. Mahoney, V. S. Kuwahara, D. D. Kolber, R. Calienes, and F. P. Chavez (2006), Primary production in the eastern tropical Pacific: A review, *Prog. Oceanogr.*, *69*(2–4), 285–317, doi:10.1016/j.pocean.2006.03.012.
Penven, P., V. Echevin, J. Pasapera, F. Colas, and J. Tam (2005), Average circulation, seasonal cycle, and mesoscale dynamics of the Peru current system: A modeling approach, *J. Geophys. Res.*, *110*, C10021, doi:10.1029/2005JC002945.
Pietri, A., P. Testor, V. Echevin, A. Chaigneau, L. Mortier, G. Eldin, and C. Grados (2013), Finescale vertical structure of the upwelling system off Southern Peru as observed from glider data, *J. Phys. Oceanogr.*, *43*(3), 631–646, doi:10.1175/JPO-D-12-035.1.
Pietri, A., V. Echevin, P. Testor, A. Chaigneau, L. Mortier, C. Grados, and A. Albert (2014), Impact of a coastal-trapped wave on the near-coastal circulation of the Peru upwelling system from glider data, *J. Geophys. Res. Oceans*, *119*, 2109–2120, doi:10.1002/2013JC009270.
Prater, M. D. (1992), Observations and hypothesized generation of a meddy in the Gulf of Cadiz, PhD thesis, Appl. Phys. Lab., Univ. of Wash., Seattle.
Revsbech, N. P., L. H. Larsen, J. Gundersen, T. Dalsgaard, O. Ulloa, and B. Thamdrup (2009), Determination of ultra-low oxygen concentrations in oxygen minimum zones by the STOX sensor, *Limnol. Oceanogr. Methods*, *7*(5), 371–381, doi:10.4319/lom.2009.7.371.
Rossi, V., C. López, J. Sudre, E. Hernández-García, and V. Garçon (2008), Comparative study of mixing and biological activity of the Benguela and Canary upwelling systems, *Geophys. Res. Lett.*, *35*, L11602, doi:10.1029/2008GL033610.
Rossi, V., C. López, E. Hernández-García, J. Sudre, V. Garçon, and Y. Morel (2009), Surface mixing and biological activity in the four eastern boundary upwelling systems, *Nonlinear Processes Geophys.*, *16*(4), 557–568, doi:10.5194/npg-16-557-2009.
Rudnick, D. L., R. E. Davis, C. C. Eriksen, D. M. Fratantoni, and M. J. Perry (2004), Underwater gliders for ocean research, *Mar. Technol. Soc. J.*, *38*(2), 73–84.
Schmidtko, S., G. C. Johnson, and J. M. Lyman (2013), MIMOC: A global monthly isopycnal upper-ocean climatology with mixed layers, *J. Geophys. Res. Oceans*, *118*, 1658–1672, doi:10.1002/jgrc.20122.
Schneider, W., R. Fuenzalida, E. Rodríguez-Rubio, J. Garcés-Vargas, and L. Bravo (2003), Characteristics and formation of eastern South Pacific intermediate water, *Geophys. Res. Lett.*, *30*(11), 1581, doi:10.1029/2003GL017086.
Silva, N., N. Rojas, and A. Fedele (2009), Water masses in the Humboldt current system: Properties, distribution, and the nitrate deficit as a chemical water mass tracer for equatorial subsurface water off Chile, *Deep Sea Res., Part II*, *56*(16), 1004–1020, doi:10.1016/j.dsr2.2008.12.013.
Smith, K. S., and R. Ferrari (2009), The production and dissipation of compensated thermohaline variance by mesoscale stirring, *J. Phys. Oceanogr.*, *39*(10), 2477–2501, doi:10.1175/2009JPO4103.1.
Stramma, L., G. C. Johnson, J. Sprintall, and V. Mohrholz (2008), Expanding oxygen-minimum zones in the tropical oceans, *Science*, *320*(5876), 655–658, doi:10.1126/science.1153847.
Stramma, L., G. C. Johnson, E. Firing, and S. Schmidtko (2010), Eastern Pacific oxygen minimum zones: Supply paths and multidecadal changes, *J. Geophys. Res.*, *115*, C09011, doi:10.1029/2009JC005976.
Stramma, L., A. Oschlies, and S. Schmidtko (2012), Mismatch between observed and modeled trends in dissolved upper-ocean oxygen over the last 50 yr, *Biogeosciences*, *9*, 4045–4057, doi:10.5194/bg-9-4045-2012.
Stramma, L., H. W. Bange, R. Czeschel, A. Lorenzo, and M. Frank (2013), On the role of mesoscale eddies for the biological productivity and biogeochemistry in the eastern tropical Pacific Ocean off Peru, *Biogeosciences*, *10*, 7293–7306, doi:10.5194/bg-10-7293-2013.
Stramma, L., R. A. Weller, R. Czeschel, and S. Bigorre (2014), Eddies and an extreme water mass anomaly observed in the eastern South Pacific at the stratus mooring, *J. Geophys. Res. Oceans*, *119*, 1068–1083, doi:10.1002/2013JC009470.
Strub, P. T., J. M. Mesias, V. Montecino, J. Rutllant., and S. Salinas (1998), Coastal ocean circulation off western South America, in *The Sea: The Global Coastal Ocean*, vol. 11, edited by A. Robinson and K. Brink, 11th ed., pp. 273–313, John Wiley, N. Y.
Testor, P., et al. (2010), Gliders as a component of future observing systems, in *Proceedings of OceanObs09: Sustained Ocean Observations and Information for Society*, vol. 2, WPP-306, Entomolog. Soc. of Am., Venice, Italy.
Thomas, L. N., J. R. Taylor, R. Ferrari, and T. M. Joyce (2013), Symmetric instability in the gulf stream, *Deep Sea Res., Part II*, *91*, 96–110, doi:10.1016/j.dsr2.2013.02.025.
Vignudelli, S., A. Kostianoy, P. Cipollini, and J. Benveniste (2011), *Coastal Altimetry*, vol. 1, Springer, Berlin.
Ward, B. B., A. H. Devol, J. J. Rich, B. X. Chang, S. E. Bulow, H. Naik, A. Pratihary, and A. Jayakumar (2009), Denitrification as the dominant nitrogen loss process in the Arabian Sea, *Nature*, *461*(7260), 78–81.

Weiss, J. (1991), The dynamics of enstrophy transfer in two-dimensional hydrodynamics, *Physica D*, *48*, 273–294.
Winkler, L. W. (1888), Die Bestimmung des im Wasser gelösten Sauerstoffes, *Ber. Dtsch. Chem. Ges.*, *21*(2), 2843–2854, doi:10.1002/cber.188802102122.
Wyrtki, K. (1962), The oxygen minima in relation to ocean circulation, *Deep Sea Res. Oceanogr. Abstr.*, *9*(1–2), 11–23, doi:10.1016/0011-7471(62)90243-7.
Wyrtki, K. (1963), The horizontal and vertical field of motion in the Peru current, *Bull. Scripps Inst. Oceanogr*, *8*, 313–344.
Wyrtki, K. (1967), Circulation and water masses in the eastern equatorial Pacific Ocean, *J. Oceanol. Limnol.*, *1*, 117–147.
Zamora, L. M., A. Oschlies, H. W. Bange, K. B. Huebert, J. D. Craig, A. Kock, and C. R. Löscher (2012), Nitrous oxide dynamics in low oxygen regions of the Pacific: Insights from the memento database, *Biogeosciences*, *9*(12), 5007–5022, doi:10.5194/bg-9-5007-2012.